

Document downloaded from:

<http://hdl.handle.net/10251/145198>

This paper must be cited as:

Pereira, A.; Santamaría Pérez, D.; Ruiz Fuertes, J.; Manjón, F.; Cuenca Gotor, VP.; Vilaplana Cerda, RI.; Gomis, O.... (26-0). Experimental and Theoretical Study of Bi₂O₂Se Under Compression. The Journal of Physical Chemistry C. 122(16):8853-8867.
<https://doi.org/10.1021/acs.jpcc.8b02194>



The final publication is available at

<https://doi.org/10.1021/acs.jpcc.8b02194>

Copyright American Chemical Society

Additional Information

Experimental and Theoretical Study of Bi₂O₂Se Under Compression

A.L.J. Pereira,^{1,2*} D. Santamaría-Pérez,³ J. Ruiz-Fuertes,^{3,4} F.J. Manjón,^{1*} V.P. Cuenca-Gotor,¹ R. Vilaplana,⁵ O. Gomis,⁵ C. Popescu,⁶ A. Muñoz,⁷ P. Rodríguez-Hernández,⁷ A. Segura,³ L. Gracia,⁸ A. Beltrán,⁹ P. Ruleova,¹⁰ C. Drasar¹⁰ and J. A. Sans¹

¹ Instituto de Diseño para la Fabricación y Producción Automatizada, MALTA Consolider Team, Universitat Politècnica de València, València, Spain

² Grupo de Pesquisa de Materiais Fotonicos e Energia Renovável - MaFER, Universidade Federal da Grande Dourados, Dourados, MS, Brazil

³ Departament de Física Aplicada – ICMUV, MALTA Consolider Team, Universitat de València, Burjassot, Spain

⁴ DCITIMAC, MALTA Consolider Team, Universidad de Cantabria, Santander, Spain

⁵ Centro de Tecnologías Físicas, MALTA Consolider Team, Universitat Politècnica de València, València, Spain

⁶ CELLS-ALBA Synchrotron Light Facility, 08290 Cerdanyola, Barcelona, Spain

⁷ Departamento de Física, Instituto de Materiales y Nanotecnología, MALTA Consolider Team, Universidad de La Laguna, Tenerife, Spain

⁸ Departament de Química Física, MALTA Consolider Team, Universitat de València, Burjassot, Spain

⁹ Departament de Química Física i Analítica, MALTA Consolider Team, Universitat Jaume I, Castellón, Spain

¹⁰ Faculty of Chemical Technology, University of Pardubice, Pardubice, Czech Republic

Abstract

We report a joint experimental and theoretical study of the structural, vibrational, elastic, optical and electronic properties of the layered high-mobility semiconductor Bi₂O₂Se at high pressure. A good agreement between experiments and *ab initio* calculations is observed for the equation of state, the pressure coefficients of the Raman-active modes and the bandgap of the material. In particular, a detailed description of the vibrational properties is provided. Unlike other Sillén-type compounds which undergo a tetragonal to collapsed tetragonal pressure-induced phase transition at relatively low pressures, Bi₂O₂Se shows a

remarkable structural stability up to 30 GPa; however, our results indicate that this compound exhibits considerable electronic changes around 4 GPa, likely related to the progressive shortening and hardening of the long and weak Bi-Se bonds linking the Bi₂O₂ and Se atomic layers. Variations of the structural, vibrational, and electronic properties induced by these electronic changes are discussed.

* Corresponding authors, Email: andreperreira@ufgd.edu.br, fjmanjon@fis.upv.es

1. Introduction

In recent years, studies related to topological insulators (TIs) have attracted the attention of many research groups. TIs are a class of quantum materials in which time-reversal symmetry, relativistic effects and an inverted band structure result in the occurrence, in an insulator bulk crystal, of electronic metallic states on the surface which are protected against non-magnetic impurities or defects. Among such materials, layered compounds Bi₂Se₃, Bi₂Te₃ and Sb₂Te₃ were predicted and found to behave as TIs¹⁻⁴. It must be stressed that TIs have promising applications in spintronic devices and dissipationless transistors based on the quantum spin Hall effect and quantum anomalous Hall effect^{5,6}, as well as to host Majorana particles⁷. In fact, TIs have already found practical applications in advanced magnetoelectronic and optoelectronic devices^{8,9}.

It has been recently suggested that there could be a close relationship between TIs and highly-efficient thermoelectric materials (TMs)¹⁰; therefore the search of new TIs is also important to find new TMs. In this context, the metal chalcogenide semiconductors belonging to the A_2X_3 (A= Sb, Bi; X= Se, Te) family with layered tetradymite structure have been of great interest mainly because of their exceptional thermoelectric (TE) properties, with Bi₂Te₃ and Sb₂Te₃ being the most widely used TMs at ambient conditions^{11,12}.

The strong interest in improving the TE properties of TMs, especially in the most interesting temperature range for TE energy harvest (between 400 and 700 K), suggests to engineer the bandgap of the materials since the optimized TMs are predicted to be semiconductors with a bandgap $E_g = 10k_B T_{op}$, where k_B is the Boltzmann constant and T_{op} is the operating temperature of TE devices¹³. Additionally, there is a strong interest in

increasing the chemical stability and in decreasing the toxicity of chalcogenide-based TMs. All the above requirements are stimulating the study of layered compounds involving heavy elements such as Bi and Sb combined with O, S and Se instead of Te. In this way, a decrease in toxicity and an increase of the chemical stability and of the bandgap will allow to reach the goal of achieving a figure of merit, ZT, near 3 in order to make a widespread use of TMs for TE energy harvest¹⁴.

Among the studied layered oxychalcogenides, Bi₂O₂Se has been found as a promising TM since it is an intrinsic n-type semiconductor with rather good TE properties around 800K¹⁵, that can be enhanced under certain stresses, as predicted by *ab initio* calculations¹⁶, or by appropriate doping^{17,18}. Most importantly, recent studies have shown that 2D nanometer-size thin films of Bi₂O₂Se exhibit an extraordinary high-mobility, which combined with its extraordinary chemical stability and large bandgap make this material a promising candidate for the realization of novel quantum phenomena, future logic devices, and flexible electronic applications^{19,20}. In fact, the application of Bi₂O₂Se films in electronic applications has been recently proved²¹. Besides, it has been recently predicted that 2D bismuth oxychalcogenides are exceptional ferroelastic/ferroelectric materials with interest in a number of applications still to be developed²².

At room pressure, Bi₂O₂Se crystallizes in a layered body-centered tetragonal structure (space group No. 139, *I4/mmm* – D_{4h}¹⁷). In this structure, Se, O and Bi atoms located at *2a* (0,0,0), *4d* (0, 1/2, 1/4) and *4e* (0,0,z) Wyckoff sites, respectively. Therefore, the *z* coordinate of the Bi atom is the only free atomic coordinate in the structure. In this structure (**Fig. 1(top)**), Bi and O atoms form Bi₂O₂ layers perpendicular to the [001] direction where Bi and O atoms are four-fold coordinated and form a square pyramid with Bi-O bond lengths of 2.3 Å. On the other hand, Se atoms form atomic layers located between the Bi₂O₂ layers. A weak link between Bi₂O₂ and Se atomic layers occurs thanks to weak Bi-Se electrostatic interactions (each Bi atom forms four Bi-Se bonds so that each Se is eightfold coordinated) with a length above 3.0 Å. In summary, the Bi₂O₂Se structure can be understood as a layered structure where Bi₂O₂ layers and Se atomic layers are 3D linked thanks to weak Bi-Se electrostatic interactions and where the lone electron pair (LEP) of each Bi atom is directed perpendicularly to the layers towards the center of the four Se atoms interacting with each Bi atom. In fact, since the closest Bi atoms of different

layers are aligned along the c axis, their corresponding LEs are facing to each other across the Se atomic layer.

A way of interpreting the structure of the Bi_2O_2 sublattice is by applying the inverse Zintl-Klemm concept^{23,24}, i.e., a “Zintl polycation” $(\text{Bi}_2\text{O}_2)^{2+}$ is formed when the two electropositive Bi atoms formally transfer 2 electrons to the Se atom. In this way, each Bi atom becomes a pseudo Ψ -Pb atom and the Bi_2O_2 sublattice adopts the same layered structure as litharge PbO (Pb_2O_2 and $(\text{Bi}_2\text{O}_2)^{2+}$ are isoelectronic)²⁵. This view is consistent with previous reports where Bi_2O_2 layers are assumed to be insulating and conductivity of $\text{Bi}_2\text{O}_2\text{Se}$ is mainly due to the large conductivity along the Se layers^{19,20}. It must be stressed that the formation of layered compounds seems to be a common feature in many Sb- and Bi-related sesquioxides and sesquichalcogenides, like the polymorphs α - Bi_2O_3 , β - Bi_2O_3 , HPC- Bi_2O_3 , Sb_2S_3 , Bi_2S_3 , Bi_2Se_3 , Sb_2Te_3 and Bi_2Te_3 ^{26,27-30}, and also in other related compounds, like BiSe, BiTe, and Bi_4Te_3 ³¹.

Pressure is a thermodynamic magnitude and a powerful tool to unravel the intrinsic properties of materials because it is cleaner than chemical doping and simpler to analyze than temperature. Therefore, the understanding of the behavior of $\text{Bi}_2\text{O}_2\text{Se}$ under compression will help to improve and fully exploit the great potential of the electronic and TE properties of this interesting material. Despite of the increasing interest in bismuth oxychalcogenides, most of the properties of layered $\text{Bi}_2\text{O}_2\text{Se}$ are barely known specially at high pressures (HPs). In this respect, it must be noted that layered compounds of the Bi_2Se_3 family studied at HP have exhibited novel phenomena such as structural phase transitions at low pressures, pressure-induced electronic topological transition (ETT) or Lifshitz transition, and pressure-induced superconductivity²⁶. Furthermore, HP exploration of Sillén-type compounds, which are isostructural to $\text{Bi}_2\text{O}_2\text{Se}$, like iron-based pnictide superconductors, have shown changes in the Fermi surface topology and new superconductor phases usually related to a tetragonal to collapsed tetragonal pressure-induced phase transition at relatively low pressures³²⁻³⁸.

In this work, we report a joint experimental and theoretical HP study of the structural, vibrational, elastic, optical, and electronic properties of $\text{Bi}_2\text{O}_2\text{Se}$ up to 30 GPa. No other study of $\text{Bi}_2\text{O}_2\text{Se}$ under compression has been previously reported to our knowledge. For that purpose, x-ray diffraction (XRD), Raman scattering (RS) and optical

absorption measurements have been combined with *ab initio* total-energy structural and lattice-dynamics calculations. It has been found that, unlike other isostructural Sillén-type compounds³²⁻³⁸, the tetragonal structure of Bi₂O₂Se presents a remarkable high stability with no phase transition up to 30 GPa. Furthermore, HP studies of both end members Bi₂O₃ and Bi₂Se₃ at high pressures show phase transitions below 30 GPa^{27-29,39}.

Curiously enough, interesting electronic changes in Bi₂O₂Se occur near 4 GPa consisting of crossing and anticrossing behaviors of the topmost and second topmost valence bands at different points of the Brillouin zone. These changes are likely related to the progressive shortening and hardening of the long and weak Bi-Se bonds between the layers. Therefore, this study will help to understand the behavior of Bi₂O₂Se and other Sillén-type compounds under compression and, in general, those of layered materials lacking van der Waals forces between their layers.

2. Experimental Method

Bi₂O₂Se polycrystalline material was recently synthesized from Bi₂Se₃ and Bi₂O₃ by solid state reaction in an evacuated quartz ampoule⁴⁰. In accordance with the literature, it was observed that the prepared samples crystallize in the space group 139, *I4/mmm* – D_{4h}¹⁷, with lattice parameters $a = 3.8859 \text{ \AA}$ and $c = 12.2055 \text{ \AA}$ and yield a unit-cell volume $V_0 = 184.30 \text{ \AA}^3$. The z atomic positions of Bi and O are: $z(\text{Bi}) = 0.355(1)$ and $z(\text{O}) = 0.250(3)$. All these parameters compare well within 0.2% with structural of ICSD-2903 entry⁴¹. This structure is the same as that of Nd₂O₂Te⁴² and the recently synthesized Bi₂O₂Te⁴³ and it is composed of insulating Bi₂O₂²⁺ layers separated by conducting square Se²⁻ atomic layers (**Fig. 1(top)**). Structural analyses have shown no spurious phases or other phases related to Bi, O or Se. On the other hand, energy-dispersive X-ray spectroscopy (EDS) analyses showed that the composition of the sample is not purely stoichiometric and has a slight excess of O and a slight deficiency of Se with respect to Bi with an approximate stoichiometry of Bi₂O_{2.2}Se_{0.8}.

Both powder angle-dispersive XRD measurements at room and HP (up 22 GPa) were performed at room temperature in an Xcalibur diffractometer with the lines K_{α1} and K_{α2} of a molybdenum source ($\lambda = 0.7093$ and 0.7136 \AA , respectively) with a Merrill-Bassett-type diamond anvil cell (DAC) with diamond culets of 400 μm in diameter⁴⁴.

Pressure was determined by the luminescence of small ruby chips evenly distributed in the pressure chamber with an error below 0.2 GPa in the whole pressure range studied⁴⁵. A more accurate powder angle-dispersive XRD experiment was also performed up to 21 GPa at room temperature in the BL04-MSPD beamline at ALBA synchrotron facility⁴⁶. This beamline is equipped with Kirkpatrick-Baez mirrors to focus the monochromatic beam and a Rayonix CCD detector with a 165 mm diameter active area and was operated with a wavelength of 0.4246 Å. Cu powder was used as the internal pressure gauge using the values $V_0 = 47.24 \text{ \AA}^3$, $B_0 = 133 \text{ GPa}$ and $B_0' = 5.01$, corresponding to a 3rd-order Vinet equation of state (EOS) which gives a pressure error below 1% in the 0-20 GPa range⁴⁷. Integration of 2D diffraction images was performed with Dioptas software⁴⁸ while structural analysis was performed by Le Bail refinements to the XRD patterns recorded at all pressures with Fullprof⁴⁹ and PowderCell⁵⁰ program packages.

Unpolarized HP-RS measurements up to 28.3 GPa were carried out with a Horiba Jobin Yvon LabRAM HR microspectrometer equipped with a thermoelectrically-cooled multichannel charge-coupled device detector which allows a spectral resolution better than 2 cm^{-1} . The signal was collected in backscattering geometry exciting with a HeNe laser (632.8 nm line) with a power of less than 10 mW. The measurements were performed at three different zones with different types of filters to assure that the sample was not burned during laser excitation. Nonetheless, it was not observed any significant difference in the spectrum apart from a change in the intensity of the peaks. Pressure was also determined by the ruby luminescence method⁴⁴. Phonons were analyzed by fitting Raman peaks with a Voigt profile fixing the Gaussian linewidth (1.6 cm^{-1}) to the experimental setup resolution.

Finally, HP optical absorption measurements at room temperature up to 19.8 GPa were performed in a plate of $\text{Bi}_2\text{O}_2\text{Se}$ 3- μm -thick and $100 \times 100 \mu\text{m}^2$ in size uniformly cleaved along the (001) plane of a single crystal. Therefore, our optical absorption measurements were performed with the electric field geometry $E \perp c$. The sample was loaded using a mixture of 16:3:1 methanol-ethanol-water together with a ruby chip for pressure calibration in a membrane-type DAC with 500 μm diamond culet anvils. The pressure chamber was in a hole of 250 μm in diameter made on an Inconel gasket preindented to 45 μm in thickness. High-pressure optical absorption experiments at room temperature were performed by the sample-in-sample-out method using a micro-optical

system^{51,52} composed of a halogen lamp, one CaF₂ lens, two Cassegrain objectives, and two spectrometers in the UV-VIS and VIS-NIR range, respectively. It must be stressed that all HP measurements were performed with a 16:3:1 methanol-ethanol-water mixture as a pressure-transmitting medium that provides hydrostatic conditions up to 10 GPa and quasi-hydrostatic conditions up to the maximum pressure attained in our experiments⁵³. Possible effects of non-purely hydrostatic conditions have been described elsewhere⁵⁴.

3. Computational Details

Ab initio total-energy calculations were performed within the framework of density functional theory (DFT)⁵⁵ to study the structural, vibrational, elastic, optical and electronic properties of Bi₂O₂Se under pressure. The Vienna Ab-initio Simulation Package (VASP)⁵⁶ was used to carry out simulations with the projector augmented wave (PAW)⁵⁷ pseudopotentials. The PAW scheme replaces core electrons and makes smoothed pseudovalence wave functions taking into account the full nodal character of the all-electron charge density in the core region. The set of plane waves employed was extended up to a kinetic energy cutoff of 520 eV due to the presence of oxygen in the compound under study. The generalized gradient approximation (GGA) was used for the description of the exchange-correlation energy within the PBEsol prescription⁵⁸. The Brillouin zone (BZ) of this body-centered tetragonal structure (with $c > a$) was sampled with a dense Monkhorst-Pack grid of special k-points⁵⁹. With the cutoff energy and the k-point sampling employed, a high convergence of 1–2 meV per formula unit in the total energy is achieved. This ensures an accurate calculation of the forces on atoms. At a set of selected volumes, the structure was fully relaxed to the optimized configuration through the calculation of the forces on atoms and the stress tensor until the forces on the atoms were smaller than 0.005 eV/Å and the deviations of the stress tensor from a diagonal hydrostatic form were lower than 0.1 GPa.

The optimized structure at different pressures was used to study the electronic properties of Bi₂O₂Se taking into account the spin orbit coupling (SOC). The band structure was analysed along the high-symmetry directions of the BZ. We want to emphasize that the BZ of Bi₂O₂Se is that of Sillén-type compounds, like SrFe₂As₂³⁸; i.e., that corresponding to a body-centered tetragonal structure (**Fig. 1(bottom)**) and not the simple tetragonal BZ

recently used in several calculations of $\text{Bi}_2\text{O}_2\text{Se}$ ^{19,22,60,61}. The path suggested for this structure (space group 139, $I4/mmm$ with $c > a$) by Bradley and Cracknell and used at the Bilbao server web page was used to plot the electronic band structure and phonon dispersion curves (PDCs)^{62,63}.

Lattice-dynamics calculations were performed to study the phonons at the Γ point of the BZ using the direct force constant approach (or supercell method). The diagonalization of the dynamical matrix provides the frequency and symmetry of the phonon modes. To obtain the PDCs, along high-symmetry directions of the BZ, and the one-phonon density of states (PDOS), similar calculations were performed using appropriate supercells, which allow the PDCs at k-points to be obtained commensurate with the supercell size⁶⁴. Finally, in order to study the HP mechanical stability of $\text{Bi}_2\text{O}_2\text{Se}$, the elastic stiffness constants were determined employing the stress theorem⁶⁵. The optimized structures were strained, at different pressures, taking into account their symmetry⁶⁶.

4. Results

4.1 Structural properties under pressure

Angle-dispersive XRD patterns of $\text{Bi}_2\text{O}_2\text{Se}$ with increasing pressure up to 22 GPa are shown in **Figure 2**. Le Bail refinements to the XRD patterns recorded at all pressures were performed using the tetragonal $I4/mmm$ structure of $\text{Bi}_2\text{O}_2\text{Se}$ (see structural data of synchrotron radiation measurements in **Table S1** in the Supplementary material). These values at 300 K are in agreement with our *ab initio* calculations at 0 K that underestimate the experimental volume by only 0.5%; i.e., well within the error margin of calculations. Noteworthy, our experimental and theoretical values are also in good agreement with those previously found in the literature¹⁵.

All diffraction peaks shift to larger angles on increasing pressure up to 22 GPa. This result is coherent with the decrease of interplanar distances at HP. No additional diffraction lines or abrupt intensity changes were observed, thus indicating the absence of a structural phase transition. Upon compression, only two interesting phenomena can be noted: i) the overlap of intense peaks related to the (103) and (110) planes above 14.5 GPa and ii) the appearance of a low-intensity peak at $\sim 11^\circ$ above 3.0 GPa (**Fig. 2**). This peak presents a large shift to high angles at HP, remains up to the maximum pressure of our study and is

not related to the $\text{Bi}_2\text{O}_2\text{Se}$ structure. In order to find the origin of this peak, we tried to refine the HP-XRD patterns using some possible structures related to elemental Bi, O and Se. In this way, this peak was tentatively assigned to the most intense reflections of the $\beta\text{-O}_2$ and $\varepsilon\text{-O}_2$ phases below and above 10 GPa, respectively^{67,68}. The high compressibility of these solid phases of oxygen would explain the large shift rate to higher angles observed in the measurements and is consistent with the excess of O found by EDS in original samples. Despite this fact, HP-XRD patterns mainly correspond to the initial tetragonal $\text{Bi}_2\text{O}_2\text{Se}$ phase up to 22 GPa, indicating that $\text{Bi}_2\text{O}_2\text{Se}$ does not present any clear phase transition. On pressure downstroke, the diffraction pattern obtained after opening the cell is identical to that of the initial sample (see top of **Fig. 2**). The lack of observation of reflections related to oxygen near room pressure on upstroke and downstroke is consistent with our hypothesis since oxygen is liquid near room conditions and no reflections from a solid phase are expected to be seen.

The pressure dependence of the experimental and theoretical lattice parameters a and c of $\text{Bi}_2\text{O}_2\text{Se}$ is shown in **Fig. 3(left)**. The axial compressibility, defined as $\kappa_x = -\frac{1}{x} \frac{\partial x}{\partial P}$ ($x = a, c$), obtained from a Birch-Murnaghan (BM) EOS fit of the experimental data⁶⁹ is reported in **Table 1** and is in good agreement with our theoretical results. Deviations of experimental lattice parameters and unit cell volume above 10 GPa with respect to theoretical estimates are likely due to non-hydrostatic stresses in the sample due to the loss of hydrostatic conditions of the pressure-transmitting medium⁵³. As expected for a 2D compound, the c -axis compressibility is much larger than the a -axis compressibility. Moreover, the c/a ratio (inset of **Fig. 3(left)**) was found to decrease smoothly with pressure in good agreement with our calculations, as it is usual in many layered materials. However, the compressibility of the c axis ($6.4 \cdot 10^{-3} \text{ GPa}^{-1}$) is much smaller than in other layered materials with van der Waals forces between the layers, like Bi_2Se_3 ($38.5 \cdot 10^{-3} \text{ GPa}^{-1}$)³⁹. This result is consistent with the larger strength of weak electrostatic interlayer Bi-Se interactions than of interlayer van der Waals forces. For completeness, the theoretical evolution of the z coordinate of Bi at HP is given at the inset of **Fig. 3(right)**. It can be observed that there is no clear change of the theoretical c/a ratio or of the z coordinate of Bi is observed in the range up to 40 GPa that could indicate a second-order pressure-induced

phase transition from a tetragonal to a collapsed tetragonal structure, unlike in other Sillén-type compounds³²⁻³⁸.

Figure 3(right) shows the experimental and theoretical pressure dependence of the unit-cell volume of Bi₂O₂Se up to 22 GPa. A 3rd-order BM EOS was used to fit our P - V data to obtain the zero pressure volume, V_0 , bulk modulus, B_0 , and its pressure derivative, B_0' , in the quasi-hydrostatic pressure range of the pressure transmitting medium (0-10 GPa). Experimental and theoretical data are summarized in **Table 1** showing rather good agreement up to 22 GPa, thus the presence of any first-order phase transition can be clearly excluded. It can be stressed that the experimental compressibility of tetragonal Bi₂O₂Se is found between that of its constituent materials, α -Bi₂O₃ ($B_0=85.4$ GPa²⁸) and layered Bi₂Se₃ ($B_0= 53$ GPa³⁹). It is noteworthy that the bulk modulus of Bi₂O₂Se is larger than that of other sesquioxides with channel-type structure, like β -Bi₂O₃ ($B_0= 34$ GPa²⁹), and larger than that of layered sesquichalcogenides, like Bi₂Se₃, Sb₂Te₃ ($B_0= 40$ GPa⁷⁰) and Bi₂Te₃ ($B_0= 40.9$ GPa⁷¹). These results can be understood by considering that Bi₂O₂Se is a layered material where Bi₂O₂ layers are separated by Se square arrays showing weak Bi-Se electrostatic interactions at room pressure instead of a standard van der Waals gap between Bi₂O₂ layers. As already commented, since the van der Waals gap is much more compressible at low pressures than weak electrostatic interactions, Bi₂O₂Se shows a smaller compressibility (larger bulk modulus) at room pressure than usual layered compounds with van der Waals gap, like those of the Bi₂Se₃ family.

The good agreement between experimental and theoretical data allows us to exploit theoretical data where experimental data are lacking. Since no reliable Rietveld refinement of XRD patterns could be performed (due to texturing effects of the polycrystalline sample) to obtain experimental atomic parameters and bond distances. **Figure 4** presents the pressure dependence of the theoretical Bi-O, Bi-Se, Se-O and interlayer Bi-Bi distances as well as of the Bi₂O₂ layer thickness. As can be observed, the Bi-O bond distance is much smaller than the Bi-Se distance at room pressure, thus indicating the strong ionic-covalent character of the Bi-O bonds and the weak electrostatic character of the Bi-Se bonds. This result justifies the fourfold coordination of Bi and the 2D character of Bi₂O₂Se at room pressure and its easy exfoliation. Regarding the pressure dependence of the bond distances, it can be observed that they decrease with increasing pressure in a monotonous way.

Notably, while the Bi-O bond distance decreases at a rate of $-4.3 \cdot 10^{-3} \text{ \AA/GPa}$ at room pressure, the Bi-Se bond distance decreases more than three times faster ($-14.8 \cdot 10^{-3} \text{ \AA/GPa}$). This strong decrease of the Bi-Se distance also correlates with the strong decrease of the Bi_2O_2 interlayer distance ($-29.5 \cdot 10^{-3} \text{ \AA/GPa}$) given by the interlayer Bi-Bi distance which results in a strong decrease of the c axis ($-78.1 \cdot 10^{-3} \text{ \AA/GPa}$). The strong decrease of the interlayer distance with pressure contrasts with the negligible decrease of the layer thickness with pressure ($-0.2 \cdot 10^{-3} \text{ \AA/GPa}$), which in turn is related to the small increase of the Bi z coordinate. Note that the Bi_2O_2 layer thickness decreases at a smaller rate than the Bi-O bond distance, thus pointing to an increase of the Bi-O-Bi angle inside the layer with pressure. For comparison with other Sillén-type compounds, the structural values found in $\text{Bi}_2\text{O}_2\text{Se}$ are between those found for SrRh_2P_2 and BaRh_2P_2 since the interlayer Bi-Bi distance (z coordinate of Bi) at room pressure is 3.59 \AA (0.354) and those for the P-P distance (z coordinate of P) in SrRh_2P_2 and BaRh_2P_2 are 3.284 \AA (0.36) and 3.737 \AA (0.351), respectively³². In these two compounds, the decrease of the interlayer P-P distance (equivalent to Bi-Bi distance in $\text{Bi}_2\text{O}_2\text{Se}$) is of $-23 \cdot 10^{-3} \text{ \AA/GPa}$ which is smaller than in $\text{Bi}_2\text{O}_2\text{Se}$. A considerable decrease of the interlayer P-P distance occurs in SrRh_2P_2 around 6 GPa from a non-bonding to a bonding state, which does not occur in BaRh_2P_2 at least up to 11 GPa; however, a phase transition at higher pressure (likely around 20 GPa) is expected when the P-P distance decreases below 3.1 \AA ³². Such bondings are typical of light elements (O, S, N, P and As), but not of heavy elements, like Bi, so a collapse of the tetragonal structure, like in SrRh_2P_2 , BaRh_2P_2 , LaCo_2P_2 , EuCo_2P_2 , EuFe_2P_2 and EuRu_2P_2 ^{32,33}, is not expected to occur in $\text{Bi}_2\text{O}_2\text{Se}$. It remains to be seen what happens in Sb-based Sillén-type compounds³⁴.

It must be stressed that despite the strong decrease of the Bi-Se distance, the value of this distance does not decrease below 3.0 \AA even up to 30 GPa, therefore, despite the Bi-Se bond length decreases and its strength hardens at HP, Bi maintains its fourfold coordination. Therefore, Bi_2O_2 layers are almost unaffected by pressure and the effect of pressure is a rather monotonous and progressive slight contraction of the Bi_2O_2 interlayer thickness. In this way, we can affirm that $\text{Bi}_2\text{O}_2\text{Se}$ still behaves as a 2D material at HP even beyond 30 GPa since there is no net increase of Bi coordination between room pressure and 30 GPa. The progressive and monotonous compression of the interlayer distance contrasts

with observations in van-der-Waals-based 2D materials, where the strong compression of the interlayer distance at low pressures is followed by a hardening of the interlayer van der Waals interactions and then results in a considerable decrease of the layer thickness. Thus, all our results on the HP behavior of Bi₂O₂Se are clearly related to the lack of a van der Waals gap between the layers and the presence of a weak electrostatic Bi-Se interaction between the layers in 2D Bi₂O₂Se.

4.3. Vibrational properties under pressure

As regards the lattice dynamics of Bi₂O₂Se, group theoretical considerations of the Bi₂O₂Se structure in the *I4/mmm* space group indicates that there are 10 normal modes of vibration at Γ whose mechanical decomposition is⁷²:

$$\Gamma = 1 A_{1g}(\text{R}) + 2 A_{2u}(\text{IR}) + 1 B_{1g}(\text{R}) + 2 E_u(\text{IR}) + 2 E_g(\text{R}) + A_{2u} + E_u$$

where A_{1g} , B_{1g} and E_g modes are Raman-active (R) and A_{2u} and E_u are infrared-active (IR). Therefore, there are four Raman-active modes ($\Gamma_{\text{Raman}} = A_{1g} + B_{1g} + 2E_g$), four infrared-active (IR) modes ($\Gamma_{\text{IR}} = 2A_{2u} + 2E_u$) and two acoustic modes ($\Gamma_{\text{Acoustic}} = A_{2u} + E_u$). Note that E modes are doubly degenerated. **Table 2** summarizes the frequencies of the experimental and theoretical vibrational modes at Γ in Bi₂O₂Se at room pressure together with the assignment of the vibrational modes to atomic movements thanks to the program J-ICE⁷³. A description of vibrational modes and its comparison with other layered materials is provided in the Supplementary Material.

RS measurements in Bi₂O₂Se at selected pressures up to 28 GPa (**Fig. 5 (left)**) show that the most intense Raman peak at room pressure is observed around 159 cm⁻¹ and, according to theoretical calculations, would correspond to the A_{1g} mode (**Fig. 5(right)**). The E_g mode, theoretically predicted at 72.0 cm⁻¹ at room pressure, is not experimentally observed at room pressure because it is in the limit of detection of our system and in a very noisy region of the RS spectrum; however, this peak is clearly seen above 3.8 GPa. It must be noted that our RS spectrum at room pressure is similar to that previously reported for bulk samples²⁰. As regards the high-frequency B_{1g} and E_g modes at room pressure, they are theoretically predicted at 369.4 cm⁻¹ and 444.0 cm⁻¹, respectively; however they were not

observed in our RS spectrum neither it was in previous measurements²⁰. Only a broad band near 350 cm^{-1} is observed which is close to the position expected for the B_{1g} mode.

At present we have no explanation for the non-observation of the high-frequency Raman-active modes of $\text{Bi}_2\text{O}_2\text{Se}$ even at room pressure. It could be due to their intrinsically small Raman scattering cross-section (RS measurements with very long exposure time and/or with high laser intensity were also performed) or to phonon damping of longitudinal optic (LO) phonons caused by the large carrier concentration in this n-type semiconductor. In this context, it could be possible that the weak broad bands observed in the high-frequency region could likely be due to plasmon-phonon coupling L^+ or L^- bands of the B_{1g} and E_g modes, as it occurs in many highly-doped semiconductors^{74,75}. A further study is needed to verify this hypothesis. It is well known that plasmon-phonon coupling severely limits the mobility of carriers⁷⁶, so this coupling could explain the rather low mobility ($\sim 150\text{ cm}^2/\text{Vs}$) found in bulk $\text{Bi}_2\text{O}_2\text{Se}$ at room temperature in comparison to low temperature where carriers are frozen¹⁹. Additional proofs have to be made in order to resolve this controversy. In case that phonon-plasmon coupling was responsible for the non-observation of high-frequency Raman modes, we propose that observation of high-frequency B_{1g} and E_g Raman-active modes at room pressure could be a good test to monitor the synthesis of $\text{Bi}_2\text{O}_2\text{Se}$ samples with low carrier concentration in order to improve the mobility of carriers at room temperature.

Since RS spectra of $\text{Bi}_2\text{O}_2\text{Se}$ up to 28.3 GPa were taken with the same power and exposure time and in the same zone of the sample, we can reasonably compare the absolute intensity of different peaks. In particular, the intensity of the A_{1g} mode decreases from 0.3 to 4.2 GPa and increases above this pressure with increasing pressure. This change of intensity is likely related to a change of the electronic polarizability due to changes of electronic origin as will be commented in the next section since they cannot be ascribed to structural changes related to the Bi LEP, unlike in other Bi-related compounds as $\beta\text{-Bi}_2\text{O}_3$ ^{29,77}. Additionally, an increase in the intensity of Raman peaks, followed by the rise of new broad bands (mainly at 154.7 cm^{-1} and in the region between 250 and 450 cm^{-1}), is observed above 10 GPa. These new bands were observed in RS measurements performed in different zones of the sample and the bands shift with increasing pressure at a similar rate to that of the first-order Raman modes (see **Figure 5(right)**), so they cannot be ascribed to

solid oxygen⁷⁸. In fact, one of them could be related to the B_{1g} vibrational mode theoretically predicted to be initially at 369.4 cm^{-1} . Since the recovered sample presents the same RS initial spectrum (see top RS spectrum in **Fig. 5(left)**), it seems that all these bands come from the sample so the hypothesis of sample decomposition is not valid to explain them. Besides, considerable disorder occurs in the sample on increasing pressure above 10 GPa, as will be discussed in the next section. Therefore, we have attributed the broad bands to second-order Raman modes and/or defect-activated Raman scattering corresponding to the PDOS as it occurs in a number of materials^{75,79,80}. A comparison of the Raman spectrum at 23.4 GPa and the PDOS at 23.7 GPa (**Figure S6** in Supplementary Material) shows that the second hypothesis is reasonable despite there are differences in frequency and intensity between the experimental and theoretical spectra which point to an overestimation of the frequencies of the high-frequency vibrational modes in theoretical calculations. It must be stressed that the RS spectrum of $\text{Bi}_2\text{O}_2\text{Se}$ after pressure release from 28.3 GPa is similar to the original one. This means that no hint of the high-frequency phonons is observed despite the possible creation of pressure-induced defects, which can behave as electron trapping centers, as it occurs in ZnO after the highly reconstructive first-order wurtzite-to-rocksalt transition⁸¹.

Figure 5(right) shows the experimental and theoretical Raman-active mode frequencies of $\text{Bi}_2\text{O}_2\text{Se}$ as a function of pressure up to 28.3 GPa and **Table 3** summarizes the experimental and theoretical frequencies and pressure coefficients of the vibrational modes of $\text{Bi}_2\text{O}_2\text{Se}$. As it can be observed, the pressure evolution of the experimental low-frequency Raman-active A_{1g} and E_g modes agrees well with our calculations despite theoretical frequencies are slightly overestimated. As it can be observed, the relative maxima of the broad band observed above 250 cm^{-1} also show similar pressure coefficients as the high-frequency modes. It is possible that the clear observation of several vibrational modes especially above 11.3 GPa could be related to the creation of defects in the sample around 10 GPa which also could be due to the loss of hydrostatic conditions of the pressure-transmitting medium and to the reduction of the phonon damping. In this context, more RS studies with samples with different n-type concentration are needed to shed light about the nature of these additional HP vibrational modes.

In summary, both HP-XRD and HP-RS measurements are in agreement with theoretical calculations and show that Bi₂O₂Se does not undergo any phase transition up to 30 GPa, unlike other isostructural Sillén-type compounds, which undergo a pressure-induced second-order tetragonal-to-collapsed tetragonal phase transition at relatively low pressures³²⁻³⁷ and lead to significant changes of vibrational and elastic properties⁸².

4.4. Dynamical and Mechanical stability of Bi₂O₂Se at HP

In order to verify that there is no hidden pressure-induced second-order phase transition, we have obtained the PDCs of Bi₂O₂Se along the main points of the BZ at 0, 12 and 23.7 GPa (**Fig. 6**). As it can be observed, there are smooth changes of vibrational frequencies with increasing pressure, but there is no softening of vibrational modes (modes whose frequency goes to zero) which could lead to think about the existence of a dynamical instability of the tetragonal phase of Bi₂O₂Se and therefore the presence of a second-order phase transition in the whole pressure range up to 25 GPa.

In a complementary way, we have calculated the pressure dependence of the elastic stiffness constants also known as elastic constants (**Figure S7** in Supplementary Material) and studied the generalized stability criteria up to 45 GPa (**Fig. 7**) for a body-centered tetragonal lattice (see Supplementary Material for more information). Evidence of a mechanical instability of the tetragonal phase of Bi₂O₂Se is only observed around 41 GPa due to the decrease of the M₂ stability criterion. This result clearly shows that the body-centered tetragonal structure of Bi₂O₂Se is mechanically stable up to 41 GPa.

In a nutshell, we can conclude that our measurements and calculations clearly support the high structural stability of the tetragonal Sillén-type phase of Bi₂O₂Se under compression and the 2D character of the compound up to 30 GPa. It must be stressed that the high structural stability of body-centered tetragonal Bi₂O₂Se could be related to the behavior of the Bi LEPs. Bi LEPs, oriented towards the atomic Se layers in Bi₂O₂Se, are likely responsible for the 2D character of many Bi-containing compounds, as already commented. It has been shown that HP leads to strong compression of Bi LEPs in other Bi-based compounds, like β -Bi₂O₃^{29,77}, and consequently leads to structural changes at relatively low pressures. Therefore, the large structural stability of layered Bi₂O₂Se can be understood by the relatively low compression of the Bi-Se distance in comparison to the

decrease of the van der Waals interlayer distance in van-der-Waals-based layered compounds. In this way, there is a small distortion of Bi LEPs at HP that prevents strong structural changes as those observed in other Bi-based compounds.

4.5. Optical Absorption Measurements

Despite the interest that TE properties of chalcogenides have attracted, the number of detailed studies regarding their optical properties is scarce. Only very recently, the indirect bandgap of Bi₂O₂Se has been determined by angle-resolved photoelectron spectroscopy (ARPES) to be around 0.8 eV¹⁹. **Figure 8** shows the optical absorption spectrum of a 3 μm-thick sample of Bi₂O₂Se at room conditions. The maximum value that the absorption coefficient reaches ($\sim 12 \cdot 10^3 \text{ cm}^{-1}$) is typical of a direct bandgap. However, the relatively slow rise of the absorption edge that extends for 0.5 eV resembles either the absorption edge of an indirect bandgap, where $\alpha \sim (h\nu - E_g)^2$, or the low-energy exponential absorption tail of a direct transition, as described by the Urbach law⁸³. In the case of Urbach's tail, the absorption coefficient can be described by $\alpha = A_0 \cdot \exp[(h\nu - E_g)/E_U]$, where A_0 is an intrinsic constant of the material, E_U is Urbach's energy and relates to the steepness of the absorption edge, and E_g is the bandgap. In the inset of **Fig. 8**, Tauc plots with the energy dependence of both the $\ln(\alpha)$ and $\alpha^{1/2}$ are shown to clarify this issue^{84,85}. We find a longer straight linear range with $\ln(\alpha)$ than with $\alpha^{1/2}$; thus suggesting that the optical bandgap of Bi₂O₂Se is most likely direct, with a value $E_g = 1.486 \text{ eV}$, and its low energy absorption tail follows an Urbach's law. This is also demonstrated by the remarkable agreement between our experimental and simulated spectra (**Fig. 8**) that provides values of $A_0 = 8300 \text{ cm}^{-1}$ and $E_U = 0.136 \text{ eV}$ once the direct bandgap value is fixed.

The theoretical electronic band structure of bulk Bi₂O₂Se calculated with DFT GGA-PBEsol including SOC at 0 GPa is shown at the top of **Figure 9**. Our calculations exhibit the minimum of the conduction band (CB) at the Γ point and the maximum of the valence band (VB) at the N point. Other two local maxima of the VB are located along the Z-X- Γ directions. According to our calculations, the bandgap of Bi₂O₂Se is indirect (N- Γ) with a value of 0.296 eV and the direct bandgaps of lower energy are located at Z (1.13 eV) and Γ (1.15 eV) points of the BZ. When compared with the indirect bandgap obtained from

ARPES measurements (0.8 eV)¹⁹, it can be observed that our calculations underestimate the indirect bandgap by 0.5 eV. Taking into account this underestimation of the bandgap, we can estimate from our calculations that the real direct optical transitions are expected around 1.4-1.6 eV; thus in good agreement with our optical absorption measurements at room pressure.

In order to study the HP behavior of the optical bandgap and check the nature of the direct gap, we have performed optical absorption experiments at HP (see **Fig. 10**). As pressure increases, the absorption edge keeps its shape and shifts to higher energies up to ~5 GPa. Above this pressure, the absorption edge becomes insensitive to pressure with the sample keeping its optical quality as evidenced by the persistence of interference fringes at the low-energy range due to the Fabry-Pérot cavity created by the sample. At ~15 GPa, in agreement with the appearance of extra vibrational bands observed before by RS spectroscopy, the fringes vanish, the low-energy tail grows, and the edge appears to shift to low energies. This might be indicative of the pressure-induced creation of defects as we will further comment. In summary, the optical bandgap of Bi₂O₂Se shows a particular behavior that can be divided into three steps. First the bandgap blueshifts up to 5 GPa with a pressure coefficient of $dE_g/dP = 29$ meV/GPa. This is followed by a pressure-independent behavior from 5 to 15 GPa and finally a redshift with $dE_g/dP = -13$ meV/GPa, accompanied by an abrupt increase of Urbach's energy.

The HP evolution of the experimental optical bandgap and Urbach's energy E_U up to 20 GPa are shown in **Fig. 11**, where they are compared to the calculated pressure dependence of the indirect N- Γ bandgap and the two lowermost direct Z-Z and Γ - Γ transitions. On one hand, the behavior of the experimental optical bandgap is qualitatively similar to that of the direct bandgap at the Γ point. In order to show it more clearly, the theoretical values have been increased by 0.34 eV so that the theoretical direct bandgap at Γ matches the experimental value of the optical direct bandgap at 0 GPa. On the other hand, the indirect transition shows a maximum at 5 GPa and then slowly redshifts with pressure, while the pressure dependence of the direct Z transition is also similar to the experimental behavior, but with a much smaller pressure coefficient. Therefore, our results confirm that Bi₂O₂Se has an indirect bandgap that can be estimated around ~0.8 eV if a shift of 0.5 eV is added to our calculations and a direct optical bandgap around 1.49 eV. The reason for not

observing optically the indirect N- Γ transition and the direct transition at Z could be related to their forbidden character (the minimum of the CB is mainly contributed by p orbitals of Bi) or to their very low absorption coefficient so that the optical direct bandgap at Γ is the one observed experimentally.

Above 15 GPa, our calculations do not reproduce the redshift experimentally observed (**Fig. 11(top)**). We believe that the experimentally observed redshifting tail is due to the progressive creation of defects above 10 GPa. The deterioration of the sample above 15 GPa is evident by the disappearance of interference fringes in the optical absorption measurements (**Fig. 10**), and Urbach's model allows us to indirectly quantify such effect with Urbach's energy E_U , as shown in **Fig. 11(bottom)**. Up to 15 GPa, E_U takes a value of ~ 160 meV, which is already high and similar to that of disordered systems as indium thiospinels^{86,87}; however, above 15 GPa, the value of E_U increases up to 240 meV at 20 GPa, which indicates that the number of defects increases abruptly above 15 GPa and making optical absorption measurements very difficult above 20 GPa. Therefore, we ascribe the decrease of the optical bandgap in Bi₂O₂Se above 15 GPa to the creation of defects that produce levels between the VB and CB, thus decreasing the optical bandgap. In this respect, the decrease of pressure allows to show the reversibility of the change of the optical bandgap, but the sample is so damaged that interference fringes are no longer observed.

It is interesting to notice the change of the pressure dependence exhibited by both the direct and indirect bandgaps between 4 and 5 GPa with an abrupt change of their pressure coefficients. In order to understand these phenomena, we have compared in **Fig. 9** the theoretical electronic band structure of bulk Bi₂O₂Se at 0 and 4.8 GPa. The electronic density of states (DOS) at both pressures is also provided as **Fig. S9** in the Supplementary material. As observed, the two topmost VBs at Γ are closer at 4.8 GPa than at 0 GPa. In fact, they cross each other around 4 GPa. This crossing explains the abrupt change in pressure coefficient of the direct gap between 4 and 5 GPa. This effect can be better seen in **Fig. 12(left)** where the pressure dependence of the orbital decomposition of the topmost VB (TVBs) and the second topmost VB (STVBs) are shown. At room pressure, the TVB in Bi₂O₂Se at Γ is mainly contributed by the p_x and p_y orbitals of Se while the STVB is mainly contributed by the p_z orbital of Se. Since STVB has a larger pressure coefficient than TVB,

they come close to each other and a crossing of these bands occurs at 4 GPa. Above that pressure, the presence of the p_x and p_y orbitals at the TVB almost decreases to zero and the p_z orbital is the main responsible for these bands at higher pressures. The contrary occurs to STVB so the energy distance between TVB and STBV increases above 4 GPa. This abrupt change is a clear indication of a band crossing. The larger pressure coefficient of the bands with p_x and p_y character is similar to that of the conduction band at Γ (also with p_x and p_y character) so the pressure coefficient of the direct bandgap above 5 GPa becomes negligible.

Similarly, the indirect bandgap N- Γ (**Fig. 11**) presents a change in the pressure coefficient (a maximum value in energy is obtained around 4.8 GPa). As in the case of the direct bandgap, the change in pressure coefficient of the N- Γ indirect bandgap can be understood by the change of the character of the two topmost VBs at the N point with increasing pressure. At ambient pressure, the TVB at the N point is mainly contributed by p_x and p_y orbitals of Se (**Fig. 12(right)**), being the p_x orbital contribution more than 10 times higher than the p_y one. On the other hand, the STVB at the N point is of the same symmetry and has similar orbital contribution of p_x and p_y orbitals of Se; however, in this case the p_y orbital contribution around 2.5 times higher than the p_x one. Since STVB have a larger pressure coefficient than TVB, they become closer in energy with increasing pressure, reaching a minimum energy distance around 5.0 GPa, and tend to separate at higher pressures. This is typical of a band anticrossing since both bands have the same character⁸⁸. At the same time, a progressive variation of the contributions of p_x and p_y orbitals of Se in both VBs occur as they come closer. In fact, the proportion of p_y character in the TVB becomes larger than that of p_x character above 5.0 GPa and the contrary occurs in the STVB, where the proportion of p_x character becomes larger than that of p_y character above 2.5 GPa. These continuous changes of character are indicative of an anticrossing of the two topmost VBs at the N point around 4 GPa. In summary, we can conclude that these crossings and anticrossings observed in the top of the VB of $\text{Bi}_2\text{O}_2\text{Se}$ are related to the high compressibility of the Bi-Se bonds as compared with the Bi-O bonds. Note that the evolution of the Bi-Se distance with pressure (**Fig. 4**) shows a pressure coefficient of $-14.8 \cdot 10^{-3} \text{ \AA/GPa}$ in the range from 0 to 4 GPa and a pressure coefficient of $-8.2 \cdot 10^{-3} \text{ \AA/GPa}$ in the range of 10 to 16 GPa; thus indicating that the bond Bi-Se becomes almost half as compressible at 10 GPa than at room pressure. This is a consequence of the 2D layered

character of $\text{Bi}_2\text{O}_2\text{Se}$ (**Fig. 1(top)**); therefore, we can ascribe the changes observed near 4 GPa in RS measurements to changes in the electronic band structure related to the strong compression of the interlayer distance and therefore affecting considerably to Se atoms. Finally, it must be stressed that the change of the character of the TVB at the N point around 4 GPa could lead to a pressure-induced electronic topological transition (ETT) if p-type doping of $\text{Bi}_2\text{O}_2\text{Se}$ is achieved.

5. Conclusions

Our joint experimental and theoretical study of the structural, vibrational, optical, elastic and electronic properties of layered $\text{Bi}_2\text{O}_2\text{Se}$ under compression has shown a good agreement between experiments and *ab initio* calculations for the EOS, the pressure coefficients of the Raman-active modes and the bandgap of this material. The compressibility and vibrational properties of this layered compound based on weak interlayer electrostatic interactions has been analyzed and discussed in comparison with typical layered compounds based on van der Waals interlayer forces. In particular, the vibrational properties of $\text{Bi}_2\text{O}_2\text{Se}$ have been discussed in detail on the light of the correct Brillouin zone for Sillén-type compounds.

No first- or second-order phase transition has been observed in $\text{Bi}_2\text{O}_2\text{Se}$ up to 30 GPa. Therefore, this material is one of the more stable Sillén-type compounds under compression. Curiously, the Bi-based compound BiSbO_4 has been recently found to be stable up to 70 GPa⁸⁹. Despite the lack of important structural changes at high pressure, $\text{Bi}_2\text{O}_2\text{Se}$ exhibits interesting electronic changes around 4 GPa, which are mainly related to the shortening and hardening of the long Bi-Se bonds, and leads to a strong change in the vibrational, optical and electronic properties of the material due to a change of the character of the topmost valence bands. We hope this work will stimulate further studies of $\text{Bi}_2\text{O}_2\text{Se}$ and will help to shed light over this high-mobility semiconductor in order to enhance the interesting electronic and TE properties of bismuth oxychalcogenides. Furthermore, the results here reported for $\text{Bi}_2\text{O}_2\text{Se}$ will be helpful to understand the properties of other layered Sillén-type compounds and in general in other layered materials lacking van der Waals forces between their layers. In particular, this study will be interesting to understand

the behavior under pressure of Sb-based Sillén-type compounds³² whose properties under pressure have not been explored to our knowledge.

Acknowledgements

This work was supported by Brazilian Conselho Nacional de Desenvolvimento Científico e Tecnológico (CNPq) under project 201050/2012-9, by Spanish MINECO projects MAT2015-71070-REDC, MAT2016-75586-C4-1/2/3-P and CTQ2015-65207-P and by the Grant Agency of the Czech Republic (GA CR) under project 16-07711S. Supercomputer time has been provided by the Red Española de Supercomputación (RES) and the MALTA cluster. D.S.-P. and J.A.S. acknowledge the “Ramón y Cajal” fellowship program and J.R.-F. the “Juan de la Cierva” program (IJCI-2014-20513) for financial support.

Supporting Information

Experimental lattice parameters and unit cell volumes of Bi₂O₂Se at different pressures. Visualization of the vibrational modes at the Γ point. Evolution with pressure of the theoretical infrared active (IR-active) modes, elastic constants, C_{ij} , and elastic stiffness, B_{ij} , of Bi₂O₂Se. Electronic Density of States (DOS) of Bi₂O₂Se at 0 GPa and 4.8 GPa.

References

1. Xia, Y.; Qian, D.; Hsieh, D.; Wray, L.; Pal, A.; Lin, H.; Bansil, A.; Grauer, D.; Hor, Y. S.; Cava, R. J.; et al. Discovery (Theoretical Prediction and Experimental Observation) of a Large-Gap Topological-Insulator Class with Spin-Polarized Single-Dirac-Cone on the Surface. *Nat. Phys.* **2009**, *5*, 398-402.
2. Zhang, H.; Liu, C. X.; Qi, X. L.; Dai, X.; Fang, Z.; Zhang, S. C. Topological Insulators in Bi₂Se₃, Bi₂Te₃ and Sb₂Te₃ With a Single Dirac Cone on the Surface. *Nat. Phys.* **2009**, *5*, 438-442.

3. Chen, Y. L.; Analytis, J. G.; Chu, J.-H.; Liu, Z. K.; Mo, S.-K.; Qi, X. L.; Zhang, H. J.; Lu, D. H.; Dai, X.; Fang, Z.; et al. Experimental Realization of a Three-Dimensional Topological Insulator, Bi₂Te₃. *Science* **2009**, *325*, 178-181.
4. Hsieh, D.; Xia, Y.; Qian, D.; Wray, L.; Meier, F.; Dil, J. H.; Osterwalder, J.; Patthey, A.; Fedorov, A. V.; Lin, H.; et al. Observation of Time-Reversal-Protected Single-Dirac-Cone Topological-Insulator States in Bi₂Te₃ and Sb₂Te₃. *Phys. Rev. Lett.* **2009**, *103*, 146401.
5. König, M.; Wiedmann, S.; Brüne, C.; Roth, A.; Buhmann, H.; Molenkamp, L. W.; Qi, X.-L.; Zhang, S.-C. Quantum Spin Hall Insulator State in HgTe Quantum Wells. *Science* **2007**, *318*, 766–770.
6. Chang, C. -Z.; Zhang, J.; Feng, X.; Shen, J.; Zhang, Z.; Guo, M.; Li, K.; Ou, Y.; Wei, P. Experimental Observation of the Quantum Anomalous Hall Effect in a Magnetic Topological Insulator. *Science* **2013**, *340*, 167–170.
7. Fu, L.; Kane, C. L. Superconducting Proximity Effect and Majorana Fermions at the Surface of a Topological Insulator. *Phys. Rev. Lett.* **2008**, *100*, 096407.
8. Yue, Z.; Cai, B.; Wang, L.; Wang, X.; Gu, M. Intrinsically Core-Shell Plasmonic Dielectric Nanostructures with Ultrahigh Refractive Index. *Sci. Adv.* **2016**, *2*, e1501536.
9. Yue, Z.; Xue, G.; Liu, J.; Wang, Y.; Gu, M. Nanometric Holograms Based on a Topological Insulator Material. *Nat. Comm.* **2017**, *8*, ncomms15354.
10. Yang, J. *Prospective Thermoelectrics among Topological Insulators, Materials Aspect of Thermoelectricity*, ed. by C. Uher, CRC, Boca Raton (USA), **2017**.
11. Rowe, D. M. *CRC Handbook of Thermoelectrics*, CRC Press Inc., New York, **1995**.

12. Venkatasubramanian, R.; Siivola, E.; Colpitts, T.; O'Quinn, B. Thin-Film Thermoelectric Devices with High Room-Temperature Figures of Merit. *Nature* **2001**, *413*, 597-602.
13. Mahan, G. D. Figure of Merit for Thermoelectrics. *J. Appl. Phys.* **1989**, *65*, 1578–1583.
14. Harman, T. C.; Taylor, P. J.; Walsh, M. P.; LaForge, B. E. Quantum Dot Superlattice Thermoelectric Materials and Devices. *Science* **2002**, *297*, 2229-2232.
15. Ruleova, P.; Drasar, C.; Lostak, P.; Li, C. P.; Ballikaya, S.; Uher, C. Thermoelectric Properties of Bi₂O₂Se. *Mater. Chem. Phys.* **2010**, *119*, 299–302.
16. Guo, D.; Hu, C.; Xi, Y.; Zhang, K. Strain Effects to Optimize Thermoelectric Properties of Doped Bi₂O₂Se via Tran – Blaha Modified Becke – Johnson Density Functional Theory. *J. Phys. Chem. C* **2013**, *117*, 21597–21602.
17. Tan, X.; Lan, J. -L.; Ren, G.; Liu, Y.; Lin, Y. -H.; Nan, C. -W. Enhanced Thermoelectric Performance of N-Type Bi₂O₂Se by Cl-Doping at Se Site. *J. Amer. Chem. Soc.* **2017**, *100*, 1494 – 1501.
18. Tan, X.; Liu, Y.; Hu, K.; Ren, G.; Li, Y.; Liu, R.; Lin, Y. -H.; Lan, J. -L.; Nan, C. -W. Synergistically Optimizing Electrical and Thermal Transport Properties of Bi₂O₂Se Ceramics by Te-Substitution. *J. Amer. Ceram. Soc.* **2018**, *101*, 326-333.
19. Wu, J.; Yuan, H.; Meng, M.; Chen, C.; Sun, Y.; Chen, Z.; Dang, W.; Tan, C.; Liu, Y.; Yin, J.; et al. High Electron Mobility and Quantum Oscillations in Non-Encapsulated Ultrathin Semiconducting Bi₂O₂Se. *Nat. Nanotech.* **2017**, *12*, 530-534.
20. Wu, J. X.; Tan, C. W.; Tan, Z. J.; Liu, Y. J.; Yin, J. B.; Dang, W. H.; Wang, M. Z.; Peng, H. L. Controlled Synthesis of High-Mobility Atomically Thin Bismuth Oxyselenide Crystals. *Nano Letters* **2017**, *17*, 3021-3026.

21. Wu, J.; Liu, Y.; Tan, Z.; Tan, C.; Yin, J.; Li, T.; Tu, T.; Peng, H. Chemical Patterning of High-Mobility Semiconducting 2D Bi₂O₂Se Crystals for Integrated Optoelectronic Devices. *Advanced Materials* **2017**, *29*, 44.
22. Wu, M.; Zeng, X. C. Bismuth Oxychalcogenides: A New Class of Ferroelectric/Ferroelastic Materials with Ultra High Mobility. *Nano Letters* **2017**, *17*, 6309-6314.
23. Shevelkov, A.V.; Shatruk, M. M. Mercury and Cadmium pnictide-halides: The Inverted Zintl Phases. *Russ. Chem. Bull. Int. Ed.* **2001**, *50*, 337-352.
24. Vegas, A.; Santamaria-Perez, D. The Structures of ZrNCl, TiOCl and AlOCl in the Light of the Zintl-Klemm Concept. *Z. Kristallogr.* **2003**, *218*, 466-469.
25. Leciejewicz, J. On the Crystal Structure of Tetragonal (red) PbO. *Acta Cryst.* **1961**, *14*, 1304.
26. Manjón, F. J.; Vilaplana, R.; Gomis, O.; Pérez-González, E.; Santamaría-Rérez, D.; Marín-Borrás, V.; Segura, A.; González, J.; Rodríguez-Hernández, P.; Muñoz, A.; et al. High-pressure Studies of Topological Insulators Bi₂Se₃, Bi₂Te₃, and Sb₂Te₃. *Phys. Stat. Sol. (b)* **2013**, *250*, 669-676.
27. Pereira, A. L. J.; Errandonea, D.; Beltrán, A.; Gracia, L.; Gomis, O.; Sans, J. A.; García-Domene, B.; Miquel-Veyrat, A.; Manjón, F. J.; Muñoz, A.; et al. Structural Study of α -Bi₂O₃ under Pressure. *J. Phys.: Cond. Mat.* **2013**, *25*, 475402.
28. Pereira, A. L. J.; Gomis, O.; Sans, J. A.; Pellicer-Porres, J.; Manjón, F. J.; Beltran, A.; Rodríguez-Hernandez, P.; Muñoz, A. Pressure Effects on the Vibrational Properties of α -Bi₂O₃: An Experimental and Theoretical Study. *J. Phys.: Cond. Mat.* **2014**, *26*, 225401.

29. Pereira, A. L. J.; Sans, J. A.; Vilaplana, R.; Gomis, O.; Manjón, F. J.; Rodríguez-Hernández, P.; Muñoz, A.; Popescu, C.; Beltrán, A. Isostructural Second-Order Phase Transition of β -Bi₂O₃ at High Pressures: An Experimental and Theoretical Study. *J. Phys. Chem. C* **2014**, *118*, 23189.
30. Ibañez, J.; Sans, J. A.; Popescu, C.; López-Vidrier, J.; Elvira-Betanzos, J. J.; Cuenca-Gotor, V. P.; Gomis, O.; Manjón, F. J.; Rodríguez-Hernández, P.; Muñoz, A. Structural, Vibrational, and Electronic Study of Sb₂S₃ at High Pressure. *J. Phys. Chem. C* **2016**, *120*, 10547.
31. Loa, I.; Bos, J.-W. G.; Downie, R. A.; Syassen, K. Atomic Ordering in Cubic Bismuth Telluride Alloy Phases at High Pressure. *Phys. Rev. B* **2016**, *93*, 224109.
32. Huhnt, C.; Michels, G.; Roepke, M.; Schlabitz, W.; Wurth, A.; Johrendt, D.; Mewis, A. First-Order Phase Transitions in the ThCr₂Si₂-type Phosphides ARh₂P₂ (A = Sr, Eu). *Phys. B: Cond. Matt.* **1997**, *240*, 26-37.
33. Huhnt, C.; Schlabitz, W.; Wurth, A.; Mewis, A.; Reehuis, M. First- and Second-Order Phase Transitions in Ternary Europium Phosphides with ThCr₂Si₂-type Structure. *Phys. B: Cond. Mat.* **1998**, *252*, 44-54.
34. Li, Y.Y.; Ni, J. The stable CaBe₂Ge₂ Structures in Antimonide Compounds ATM₂Sb₂ (A = Ca, Sr, Ba; TM = Fe, Co, Ni, Cu): A First-Principles Study. *Phys. Lett. A* **2011**, *375*, 4218-4224.
35. Sefat, A. S. Pressure Effects on Two Superconducting Iron-Based Families. *Rep. Prog. Phys.* **2011**, *74*, 124502-124516.

36. Sun, L.; Chen, X.-J.; Guo, J.; Gao, P.; Huang, Q.-Z.; Wang, H.; Fang, M.; Chen, X.; Chen, G.; Wu, Q.; Zhang, C.; et al. Re-Emerging Superconductivity at 48 Kelvin in Iron Chalcogenides. *Nature* **2012**, *483*, 67–69.
37. Das, T.; Balatsky, A. V. Origin of Pressure Induced Second Superconducting Dome in $A_y\text{Fe}_{2-x}\text{Se}_2$ [$A = \text{K}, (\text{Tl}, \text{Rb})$]. *New J. Phys.* **2013**, *15*, 093045-093057.
38. Wang, Y. Q.; Lu, P. C.; Wu, J. J.; Liu, J.; Wang, X. C.; Zhao, J. Y.; Bi, W.; Alp, E. E.; Park, C. Y.; Popov, D.; et al. Phonon Density of States of Single-Crystal SrFe_2As_2 across the Collapsed Phase Transition at High Pressure. *Phys. Rev. B* **2016**, *94*, 014516.
39. Vilaplana, R.; Santamaría-Pérez, D.; Gomis, O.; Manjón, F. J.; González, J.; Segura, A.; Muñoz, A.; Rodríguez-Hernández, E.; Pérez-González, E.; Marín-Borrás, V.; et al. Structural and Vibrational Study of Bi_2Se_3 under High Pressure. *Phys. Rev. B* **2011**, *84*, 184110.
40. Ruleova, P.; Drasar, C.; Benes, L.; Lostak, P.; Li, C.-P.; Kong, H.; Uher, C. $\text{Bi}_2\text{O}_2\text{Se}$ – A Prospective Thermoelectric Material? *6th Eur. Conf. Thermoelectr.* **2009**, P2-35.
41. Boller, H. Die Kristallstruktur von $\text{Bi}_2\text{O}_2\text{Se}$. *Monatshefte fuer Chemie* **1973**, *104*, 916-919.
42. Raccah, P. M.; Longo, J. M.; Eick, H. A. The Crystal Structure of Neodymium Monotellurooxide- $\text{Nd}_2\text{O}_2\text{Te}$. *Inorg. Chem.* **1967**, *6*, 1471–1473.
43. Luu, S. D. N.; Vaqueiro, P. Synthesis, Characterization and Thermoelectric Properties of the Oxytelluride $\text{Bi}_2\text{O}_2\text{Te}$. *J. Sol. State Chem.* **2015**, *226*, 219–223.
44. Merrill, L.; Bassett, W.A. Miniature Diamond Anvil Pressure Cell for Single Crystal X-Ray Diffraction Studies. *Rev. Sci. Instr.* **1974**, *45*, 290-294.

45. Mao, H. K.; Xu, J.; Bell, P. M. Calibration of the Ruby Pressure Gauge to 800 Kbar under Quasi-Hydrostatic Conditions. *J. Geophys. Res.* **1986**, *91*, 4673 - 4676.
46. Fauth, F.; Peral, I.; Popescu, C.; Knapp, M. The New Material Science Powder Diffraction Beamline at ALBA Synchrotron. *Powder Diffr.* **2013**, *28*, S360 – S370.
47. Dewaele, A.; Loubeyre, P.; Mezouar, M. Equations of State of Six Metals Above 94 GPa. *Phys. Rev. B* **2004**, *70*, 094112.
48. Prescher, C.; Prakapenka, V. B. DIOPTAS: A Program for Reduction of Two-Dimensional X-Ray Diffraction Data and Data Exploration. *High Press. Res.* **2015**, *35*, 223-230.
49. Rodriguez-Carvajal, J. Recent Advances in Magnetic Structure Determination by Neutron Powder Diffraction. *Phys. B: Cond.Mat.* **1993**, *192*, 55–69.
50. Nolze, G.; Kraus, W. PowderCell 2.0 for Windows. *Powder Diffr.* **1998**, *13*, 256–259.
51. Letoullec, R.; Pinceaux, J. P.; Loubeyre, P. The Membrane Diamond Anvil Cell: A New Device for Generating Continuous Pressure and Temperature Variations. *High Press. Res.* **1988**, *1*, 77-90.
52. Goñi, A. R.; Syassen, K. *High Pressure Semiconductor Physics I*, Chapter 4, Ed. T. Suski and W. Paul, Academic Press **1998**.
53. Klotz, S.; Chervin, J.-C.; Munsch, P.; Le Marchand, G. Hydrostatic Limits of 11 Pressure Transmitting Media. *J. Phys. D: Appl. Phys.* **2009**, *42*, 075413-1 – 075413-7.
54. Errandonea, D.; Muñoz, A.; Gonzalez-Platas, J. Comment on “High-Pressure X-Ray Diffraction Study of $\text{YBO}_3/\text{Eu}^{3+}$, GdBO_3 , and EuBO_3 : Pressure-Induced Amorphization in GdBO_3 ”. *J. Appl. Phys.* **2014**, *115*, 043507]. *J. Appl. Phys.* **2014**, *115*, 216101.

55. Hohenberg, P.; Kohn, W. Inhomogeneous Electron Gas. *Phys. Rev.* **1964**, *136*, 864–871.
56. Kresse, G.; Hafner, J. Ab Initio Molecular Dynamics for Liquid Metals. *Phys. Rev. B* **1993**, *47*, 558–561.
57. Blöchl, P. E. Projector Augmented-Wave Method. *Phys. Rev. B* **1994**, *50*, 17953–17979.
58. Perdew, J. P.; Ruzsinszky, A.; Csonka, G. I.; Vydrov, O. A.; Scuseria, G. E.; Constantin, L. A.; Zhou, X.; Burke, K. Restoring the Density-Gradient Expansion for Exchange in Solids and Surfaces. *Phys. Rev. Lett.* **2008**, *100*, 136406.
59. Monkhorst, H.J.; Pack, J.D. Special Points for Brillouin-zone integrations. *Phys. Rev. B* **1976**, *13*, 5188-5192.
60. Van Quang, T.; Lim, H.; Kim, M. Temperature and Carrier-Concentration Dependences of the Thermoelectric Properties of Bismuth Selenide Dioxide Compounds. *J. Kor. Phys. Soc.* **2012**, *61*, 1728-1731.
61. Van Quang, T.; Kim, M. Role of O and Se Defects in the Thermoelectric Properties of Bismuth Oxide Selenide. *J. Appl. Phys.* **2016**, *120*, 195105-1 – 195105-5.
62. Bradley, C. J.; Cracknell, A. P. *The Mathematical Theory of Symmetry in Solids*. Clarendon Press. Oxford, **1972**.
63. Aroyo, M. I.; Orobengoa, D.; de la Flor, G.; Tasci, E. S.; Perez-Mato, J. M.; Wondratschek, H. Brillouin-zone Database on the Bilbao Crystallographic Server. *Acta Cryst. A* **2014**, *70*, 126 -137.
64. Parlinski, K. Computer Code PHONON. See: <http://wolf.ifj.edu.pl/phonon>.
65. Nielsen, O.H.; Martin, R.M. Quantum-mechanical Theory of Stress and Force. *Phys. Rev. B* **1985**, *32*, 3780–3791.

66. Le Page, Y.; Saxe, P. Symmetry General Least-Squares Extraction of Elastic Data for Strained Materials From ab Initio Calculations of Stress. *Phys. Rev. B* **2002**, *65*, 104104.
67. Fujihisa, H.; Akahama, Y.; Kawamura, H.; Ohishi, Y.; Shimomura, O.; Yamawaki, H.; Sakashita, M.; Gotoh, Y.; Takeya, S.; Honda, K. O₈ Cluster Structure of the Epsilon Phase of Solid Oxygen. *Phys. Rev. Lett.* **2006**, *97*(8), 085503.
68. Lundergaard, L. F.; Weck, G.; McMahon, M. I.; Desgreniers, S.; Loubeyre, P. Observation of an O₈ Molecular Lattice in the Epsilon Phase of Solid Oxygen. *Nature* **2006**, *443*, 201–204.
69. Birch, F. J. Finite Strain Isotherm and Velocities for Single-Crystal and Polycrystalline NaCl at High Pressures and 300K. *Geophys. Res.* **1978**, *83*, 1257-1268.
70. Sakai, N.; Kajiwara, T.; Takemura, K.; Minomura, S.; Fujii, Y. Pressure-Induced Phase Transition in Sb₂Te₃. *Sol. State Commun.* **1981**, *40*, 1045-1047.
71. Polian, A.; Gauthier, M.; Souza, S. M.; Triches, D. M.; Cardoso de Lima, J.; Grandi, T. A. Two-Dimensional Pressure-Induced Electronic Topological Transition in Bi₂Te₃. *Phys. Rev. B* **2011**, *83*, 113106.
72. Kroumova, E.; Aroyo, M. I.; Perez Mato, J. M.; Kirov, A.; Capillas, C.; Ivantchev, S.; Wondratschek, H. Bilbao Crystallographic Server: Useful Databases and Tools for Phase Transitions Studies. *Phase Transitions* **2003**, *76*, 155-170.
73. Canepa, P.; Hanson, R. M.; Ugliengo, P.; Alfredsson, M. J-ICE: A New Jmol Interface for Handling and Visualizing Crystallographic and Electronic Properties. *J. Appl. Cryst.* **2011**, *44*, 225-229.

74. Lockwood, D. J.; Yu, G.; Rowell, N. L. Optical Phonon Frequencies and Damping in AlAs, GaP, GaAs, InP, InAs and InSb Studied by Oblique Incidence Infrared Spectroscopy. *Sol. State Comm.* **2005**, *136*, 404-409.
75. Ibáñez, J.; Oliva, R.; Manjón, F. J.; Segura, A.; Yamaguchi, T.; Nanishi, Y.; Cusco, R.; Artus, L. High-Pressure Lattice Dynamics in Wurtzite and Rocksalt Indium Nitride Investigated by Means of Raman Spectroscopy. *Phys. Rev. B* **2013**, *88*, 115202.
76. Hauber, A.; Fahy, S. Scattering of Carriers by Coupled Plasmon-Phonon Modes in Bulk Polar Semiconductors and Polar Semiconductor Heterostructures. *Phys. Rev. B* **2017**, *95*, 045210.
77. Pereira, A. L. J.; Gomis, O.; Sans, J. A.; Contreras-García, J.; Manjón, F. J.; Rodríguez-Hernández, P.; Muñoz, A.; Beltrán, A. β -Bi₂O₃ Under Compression: Optical and Elastic Properties and Electron Density Topology Analysis. *Phys. Rev. B* **2016**, *93*, 224111-1 – 224111-13.
78. Akahama, Y.; Kawamura, H. High-Pressure Raman Spectroscopy of Solid Oxygen. *Phys. Rev. B* **1996**, *54*, R15602 - R15605.
79. Halsall, M. P.; Harmer, P.; Parbrook, P. J.; Henley, S. J. Raman Scattering and Absorption Study of the High-Pressure Wurtzite to Rocksalt Phase Transition of GaN. *Phys. Rev. B* **2004**, *69*, 235207.
80. Manjón, F. J.; Errandonea, D.; Romero, A. H.; Garro, N.; Serrano, J.; Kuball, M. Lattice Dynamics of Wurtzite and Rocksalt AlN Under High Pressure: Effect of Compression on the Crystal Anisotropy of Wurtzite-Type Semiconductors. *Phys. Rev. B* **2008**, *77*, 205204.

81. Manjón, F. J.; Syassen, K.; Lauck, R. Effect of Pressure on Phonon Modes in Wurtzite Zinc Oxide. *High Pres. Res.* **2002**, *22*, 299-304.
82. Wang, Y. Q.; Lu, P. C.; Wu, J. J.; Liu, J.; Wang, X. C.; Zhao, J. Y.; Bi, W.; Alp, E. E.; Park, C. Y.; Popov, D.; et al. Phonon Density of States of Single-Crystal SrFe₂As₂ across the Collapse Phase Transition at High Pressure. *Phys. Rev. B* **2016**, *94*, 014516.
83. Urbach, F. The Long-Wavelength Edge of Photographic Sensitivity and of the Electronic Absorption of Solids. *Phys. Rev.* **1953**, *92*, 1324.
84. Tauc, J. Optical Properties and Electronic Structure of Amorphous Ge and Si. *Mater. Res. Bull.* **1968**, *3*, 37–46.
85. Errandonea, D.; Muñoz, A.; Rodríguez-Hernández, P.; Proctor, J. E.; Sapiña, F.; Bettinelli, M. Theoretical and Experimental Study of the Crystal Structures, Lattice Vibrations, and Band Structures of Monazite-Type PbCrO₄, PbSeO₄, SrCrO₄, and SrSeO₄. *Inorg. Chem.*, **2015**, *54* (15), 7524–7535.
86. Ruiz-Fuertes, J.; Errandonea, D.; Manjón, F. J.; Martínez-García, D.; Segura, A.; Ursaki, V. V.; Tiginyanu, I. M. High-Pressure Effects on the Optical-Absorption Edge of CdIn₂S₄CdIn₂S₄, MgIn₂S₄MgIn₂S₄, and MnIn₂S₄MnIn₂S₄ Thiospinels. *J. Appl. Phys.* **2008**, *103*, 063710.
87. Santamaria-Perez, D.; Ruiz-Fuertes, J. *AB₂S₄ and AB₂Se₄ Compounds at High Pressures. in Pressure-Induced Phase Transitions in AB₂X₄ Chalcogenide Compounds.* Springer Verlag., 75-102, **2014**.
88. Manjón, F. J.; Gomis, O.; Rodríguez-Hernández, P.; Pérez-González, E.; Muñoz, A.; Errandonea, D.; Ruiz-Fuertes, J.; Segura, A.; Fuentes-Cabrera, M.; Tiginyanu, I. M.; et al. Nonlinear Pressure Dependence of the Direct Band Gap in Adamantine Ordered-Vacancy Compounds. *Phys. Rev. B* **2010**, *81*, 195201.

89. Errandonea, D.; Muñoz, A.; Rodríguez-Hernández, P.; Gomis, O.; Achary, S. N.; Popescu, C.; Patwe, S. J.; Tyagi, A. K. High-Pressure Crystal Structure, Lattice Vibrations, and Band Structure of BiSbO₄. *Inorg. Chem.* **2016**, *55* (10), 4958–4969.

Tables

Table 1 - EOS parameters and axial compressibilities of Bi₂O₂Se at room pressure.

	V_0 (Å ³)	B_0 (GPa)	B_0'	κ_a (10 ⁻³ GPa ⁻¹)	κ_c (10 ⁻³ GPa ⁻¹)
Experimental	184.69(8)	71.5(13)	5.6(3)	3.6(2)	6.4(2)
Theoretical	183.8	88.17	4.86	3.0	5.9

Table 2 - Experimental and theoretical Raman (R) and infrared (IR) mode frequencies of Bi₂O₂Se at room pressure.

Symmetry	Exp. Freq. (cm ⁻¹)	Theor. Freq. (cm ⁻¹)	Assignment
E_u (IR)		59.2	Bi and Se out-of-phase movement along the layer (shear interlayer mode)
A_{2u} (IR)		64.5	Bi and Se out of-phase movement perpendicular to the layer (longitudinal interlayer mode)
E_g (R)		72.0	Bi out-of-phase interlayer movement along the layer
A_{1g} (R)	159.2	165.7	Bi out-phase interlayer movement perpendicular to the layers (breathing mode of the layers)
E_u (IR)		293.9	O in-phase intralayer movement along the layer
B_g (R)		369.4	O out-of-phase intralayer movement perpendicular to the layer
A_{2u} (IR)		402.8	O in-phase intralayer movement perpendicular to the layer
E_g (R)		444.0	O out-of-phase intralayer movement along the layer

Table 3 – Experimental and theoretical first-order Raman (R) and infrared (IR) vibrational mode frequencies and pressure coefficients at room pressure in Bi₂O₂Se as obtained by a fit with the equation $\omega(P) = \omega_0 + a \cdot P$ in the pressure range from 0 to 4 GPa. The frequencies and pressure coefficients of other modes observed at different pressures (indicated) are also provided.

Symmetry	Experimental		Theoretical	
	ω_0 (cm ⁻¹)	a (cm ⁻¹ /GPa)	ω_0 (cm ⁻¹)	a (cm ⁻¹ /GPa)
E_u (IR)			59.2(3)	5.5(2)
A_{2u} (IR)			64.5(1)	4.1(9)
E_g (R)	59.5(5)	1.0(2)	72.0(1)	1.1(8)
A_{1g} (R)	160.5(6)	2.1(3)	165.7(3)	2.1(2)
E_u (IR)			293.9(1)	4.2(6)
B_g (R)			369.4(5)	4.0(5)
A_{2u} (IR)			402.8(6)	3.1(4)
E_g (R)			444.0(1)	5.3(7)
P1 (6.6 GPa)	137(3)	1.9(4)		
P2 (10.0 GPa)	280(8)	1.1(5)		
P3 (10.0 GPa)	285(7)	2.6(4)		
P4 (6.6 GPa)	296(4)	4.0(2)		
P5 (10.0 GPa)	381(7)	1.8(3)		
P6 (10.0 GPa)	447(5)	2.5(2)		
P7 (10.0 GPa)	537(8)	0.4(4)		
P8 (10.0 GPa)	568(6)	1.2(2)		

Figure Captions

Figure 1. (color online) (top) Crystalline structure of tetragonal $\text{Bi}_2\text{O}_2\text{Se}$ at 1 atm. Large magenta balls represent Bi atoms, while small red balls represent O atoms and medium-sized green balls represent Se atoms. Bi atoms are linked to four O atoms with short bonds (solid lines) and to four Se atoms with long bonds (dashed lines). O atoms are surrounded by four Bi atoms and Se atoms are surrounded by eight Bi atoms. The structure is composed by alternate Bi_2O_2 layers, where Bi atoms show fourfold coordination, and atomic Se layers. (bottom) Brillouin zone of the body-centered tetragonal unit cell with $c/a > 1$.

Figure 2. (color online) Angle-dispersive XRD patterns of $\text{Bi}_2\text{O}_2\text{Se}$ measured at different pressures up to 22 GPa at room temperature and on decreasing pressure to room pressure (top pattern). The low-pressure patterns (in circles) include the calculated LeBail (black line) and difference (red line) XRD profiles. Blue and black vertical markers indicate the Bragg reflections of the tetragonal $\text{Bi}_2\text{O}_2\text{Se}$ phase and the Cu pressure gauge, respectively.

Figure 3. (color online) Experimental (symbols) and theoretical (lines) pressure dependence of the lattice parameters a and c (left) and of the unit-cell volume (right) for $\text{Bi}_2\text{O}_2\text{Se}$. Insets show the pressure dependence of the z coordinate of Bi atoms (left) and the c/a ratio (right). Experimental data include those from our in-home Xcalibur diffractometer (squares) and from the ALBA-CELLS beamline (circles). Errors in the determination of parameters are indicated by symbol sizes. In the volume plot, the solid black line is the EOS fit to the theoretical data while the dashed red line is the EOS fit to experimental data in the quasi-hydrostatic pressure range.

Figure 4. (color online) Pressure dependence of the theoretical interatomic and interplanar distances in $\text{Bi}_2\text{O}_2\text{Se}$.

Figure 5. (color online) (left) Room-temperature Raman spectra of $\text{Bi}_2\text{O}_2\text{Se}$ at selected pressures up to 28.3 GPa. The top spectrum corresponds to the recovered sample after decompression. (right) Experimental (symbols) and theoretical (lines) pressure dependence

of the Raman-active modes of Bi₂O₂Se. Different colors represent Raman-active modes of different symmetries.

Figure 6. Theoretical PDCs of Bi₂O₂Se at 0 GPa (top), 12 GPa (center), and 23.7 GPa (bottom) following the path: X (0,0,½) - Γ (0,0,0) - Z (½,½,-½) - P (¼,¼,¼) - N (0, ½,0).

Figure 7. Pressure dependence of generalized stability criteria of Bi₂O₂Se up to 45 GPa.

Figure 8. (color online) Optical absorption spectrum (black) of Bi₂O₂Se at ambient pressure fitted to a direct-type Urbach law (red). The inset shows the linear range presented by the absorption edge of Bi₂O₂Se considering either an indirect ($\alpha^{1/2}$) or a direct-type Urbach tail ($\ln(\alpha)$). The points are experimental data while the straight red lines are guides for the eye.

Figure 9. (color online) Electronic band structure of Bi₂O₂Se at (top) 0 GPa and 4.8 GPa (bottom) following the path: X (0,0,½) - Γ (0,0,0) - Z (½,½,-½) - P (¼,¼,¼) - N (0, ½,0). Topmost valence bands (in red) and second topmost valence bands (in blue) are colored in order to better show the crossing and anticrossing taking place in these bands with increasing pressure around 4 GPa.

Figure 10. (color online) Optical absorption edge of Bi₂O₂Se on increasing pressure up to 20 GPa.

Figure 11. (Color online) (top) Pressure dependence of the band gap of Bi₂O₂Se obtained from fitting the absorption edge to the Urbach's law. Dots represent the experimental data and the continuous lines are the calculated dependences for the $\Gamma \rightarrow \Gamma$ (red line) and the $Z \rightarrow Z$ (blue line) direct transitions after adding +0.34 eV to compare to the experimentally observed bandgap at ambient pressure. The theoretical N- Γ indirect bandgap of Bi₂O₂Se is also shown for comparison (pink line). (bottom) Pressure dependence of the Urbach energy in Bi₂O₂Se.

Figure 12. Pressure evolution of the Se orbitals contribution in the top valence bands at (left) Γ and (right) N points. The sudden change of character of topmost valence bands at Γ is indicative of a band crossing while the progressive change of character of topmost valence bands at N is indicative of a band anticrossing.

Figure 1(top)

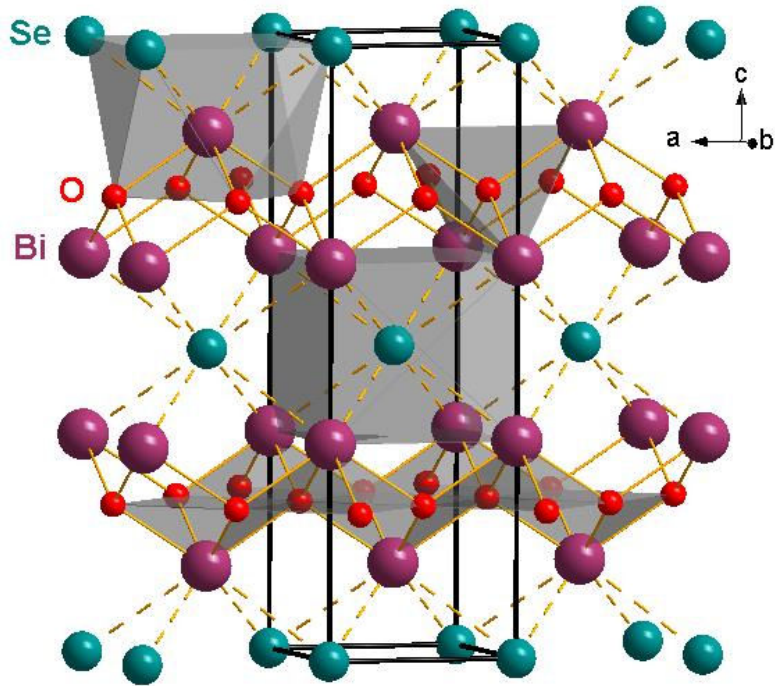


Figure 1(bottom)

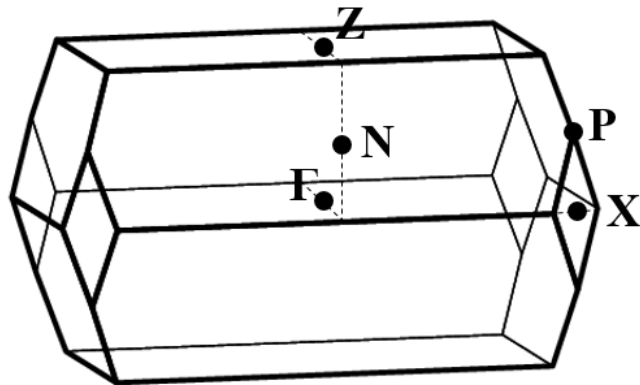


Figure 2

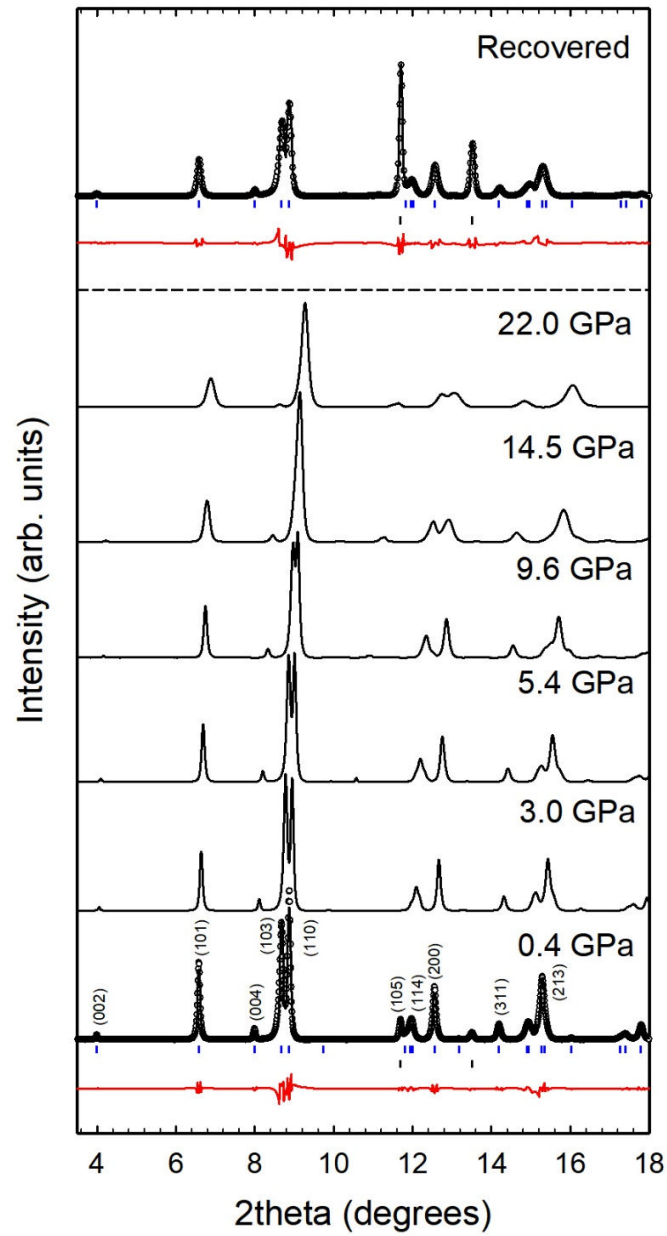


Figure 3(left)

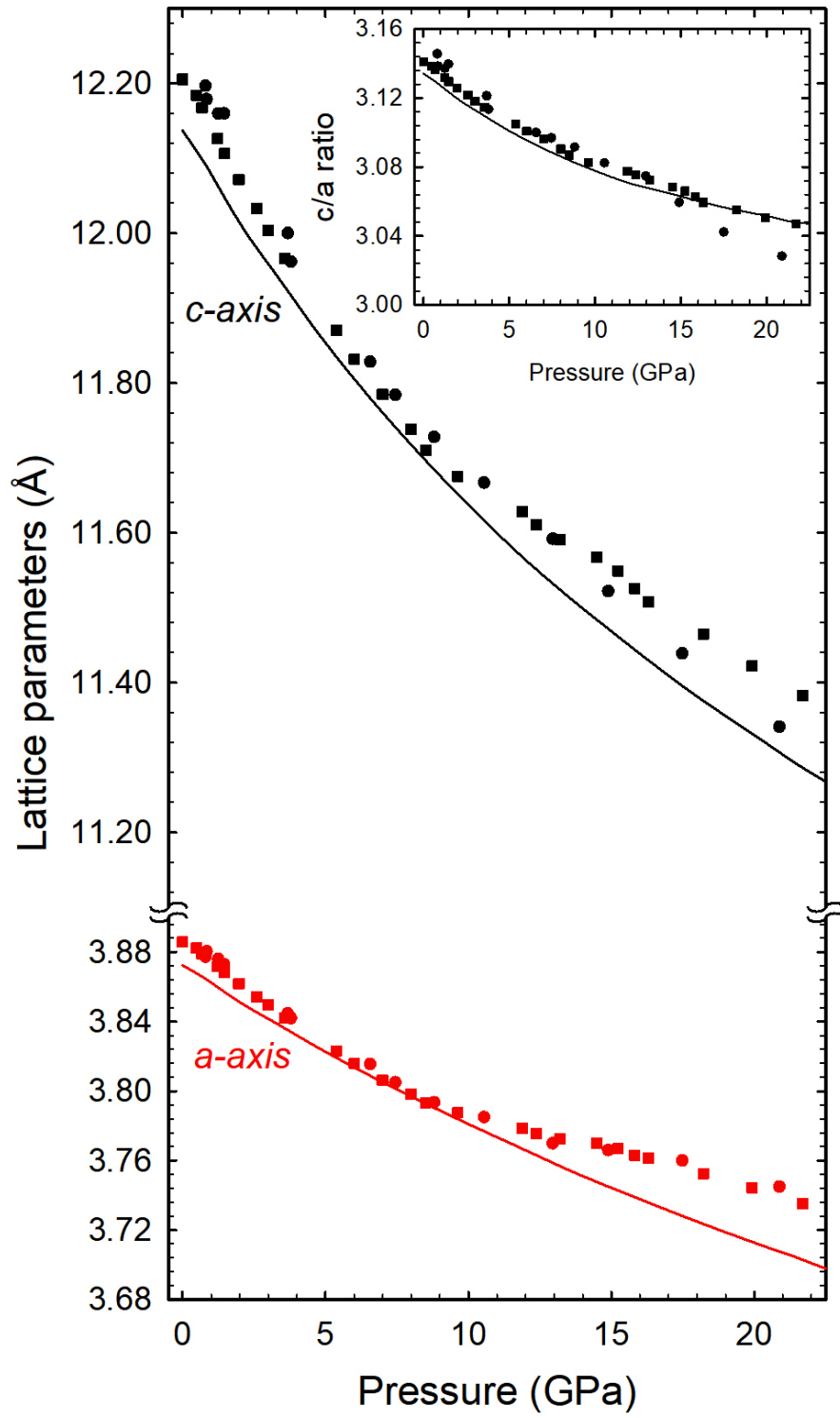


Figure 3(right)

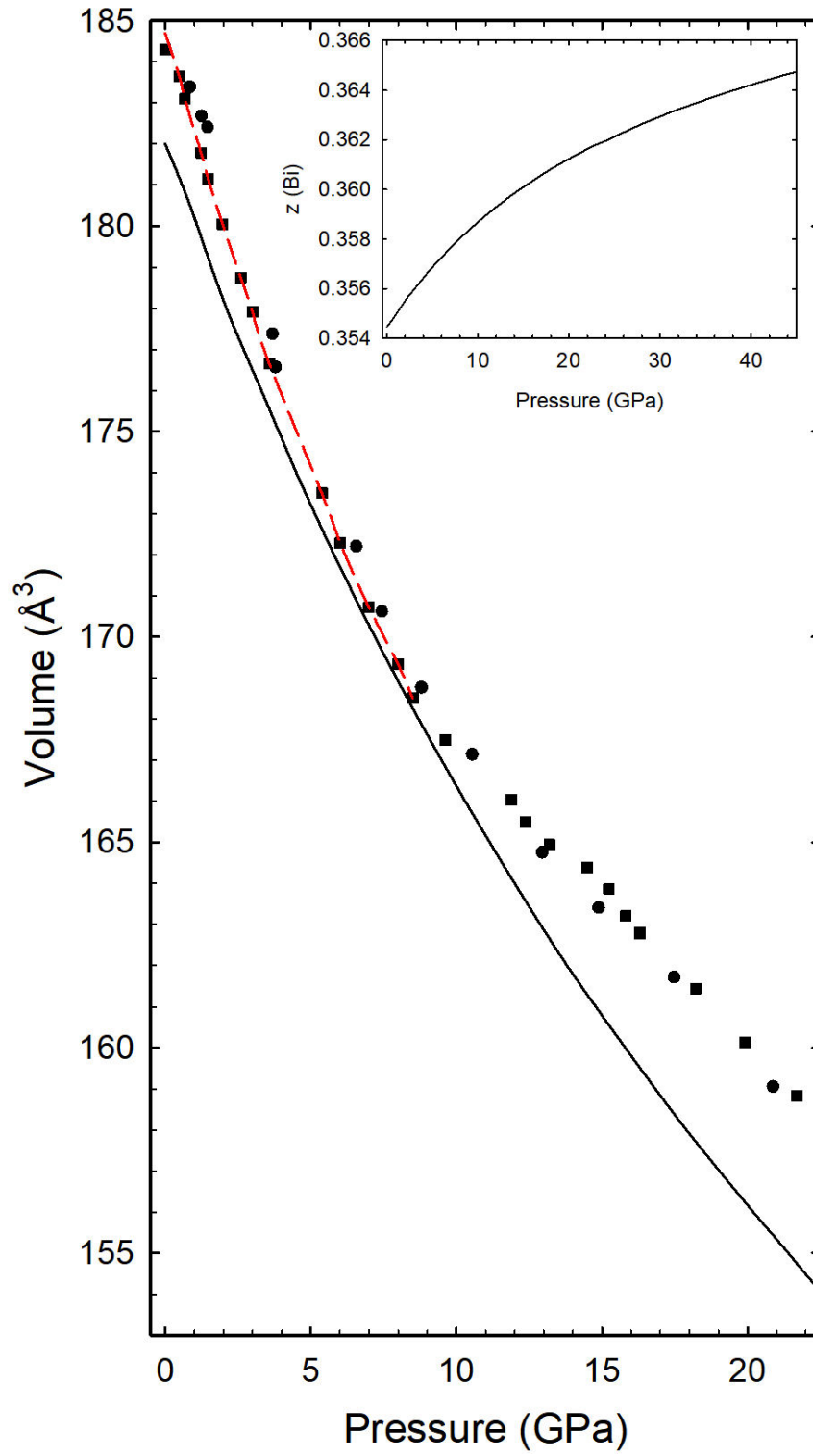


Figure 4

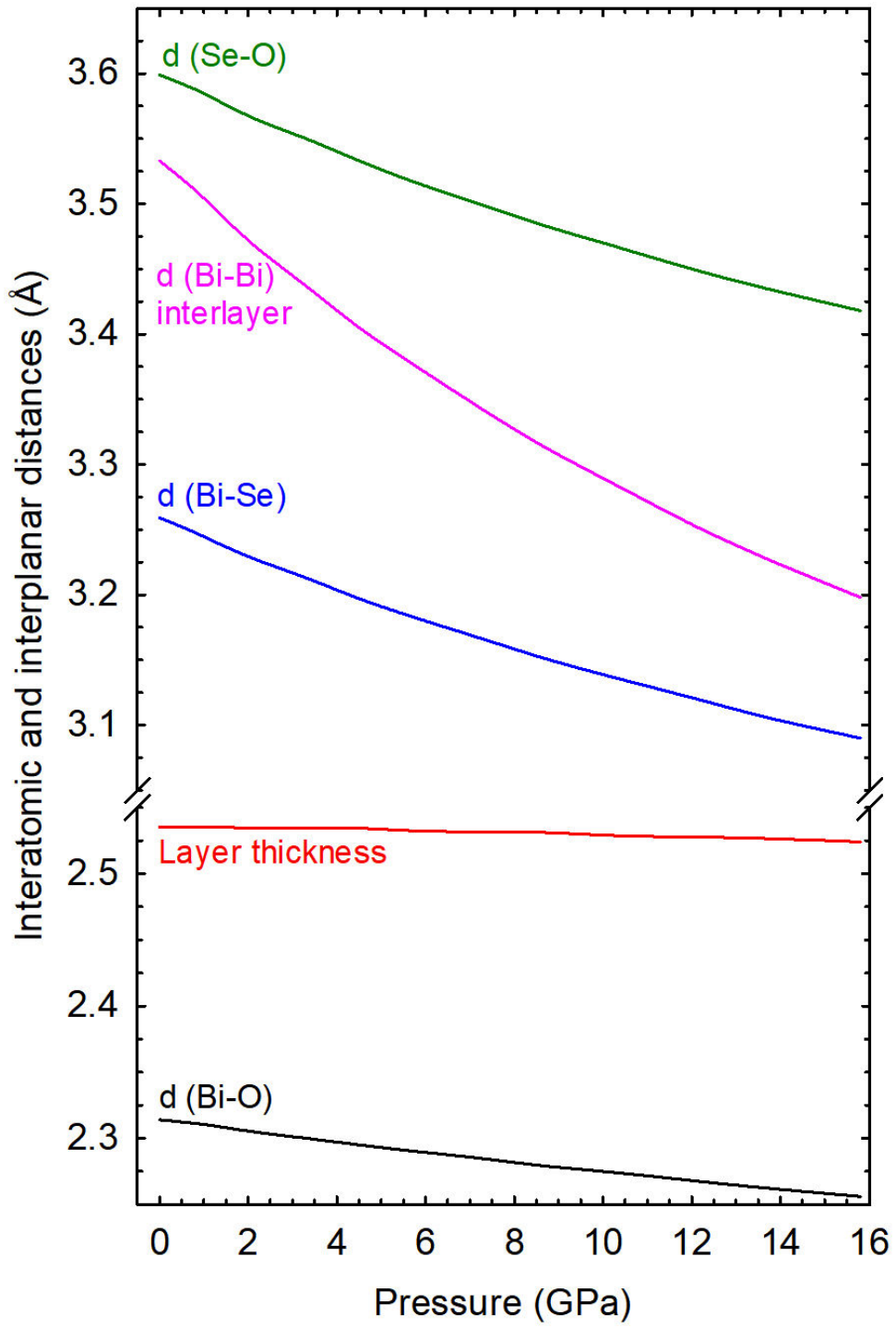


Figure 5 (left)

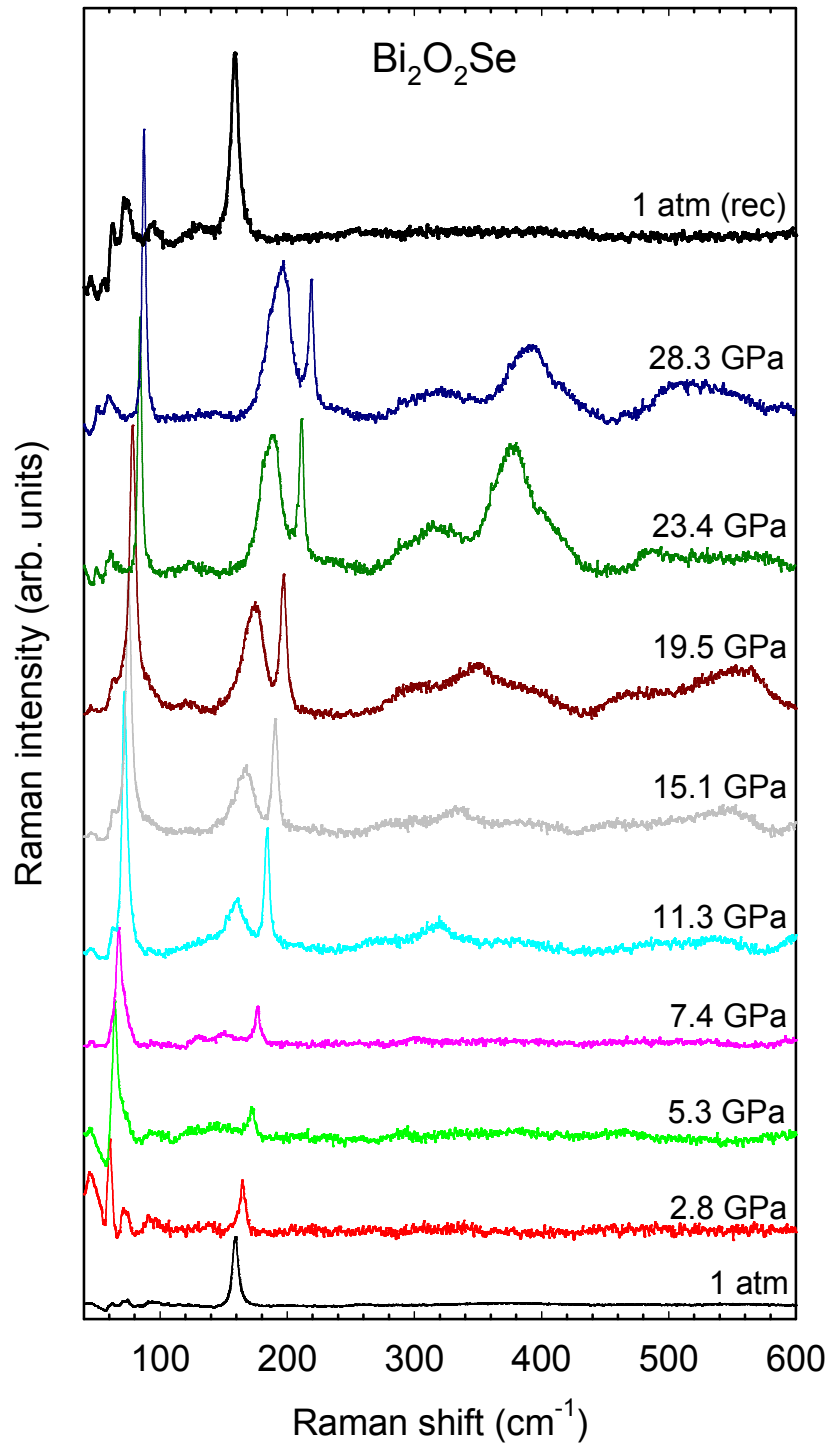


Figure 5 (right)

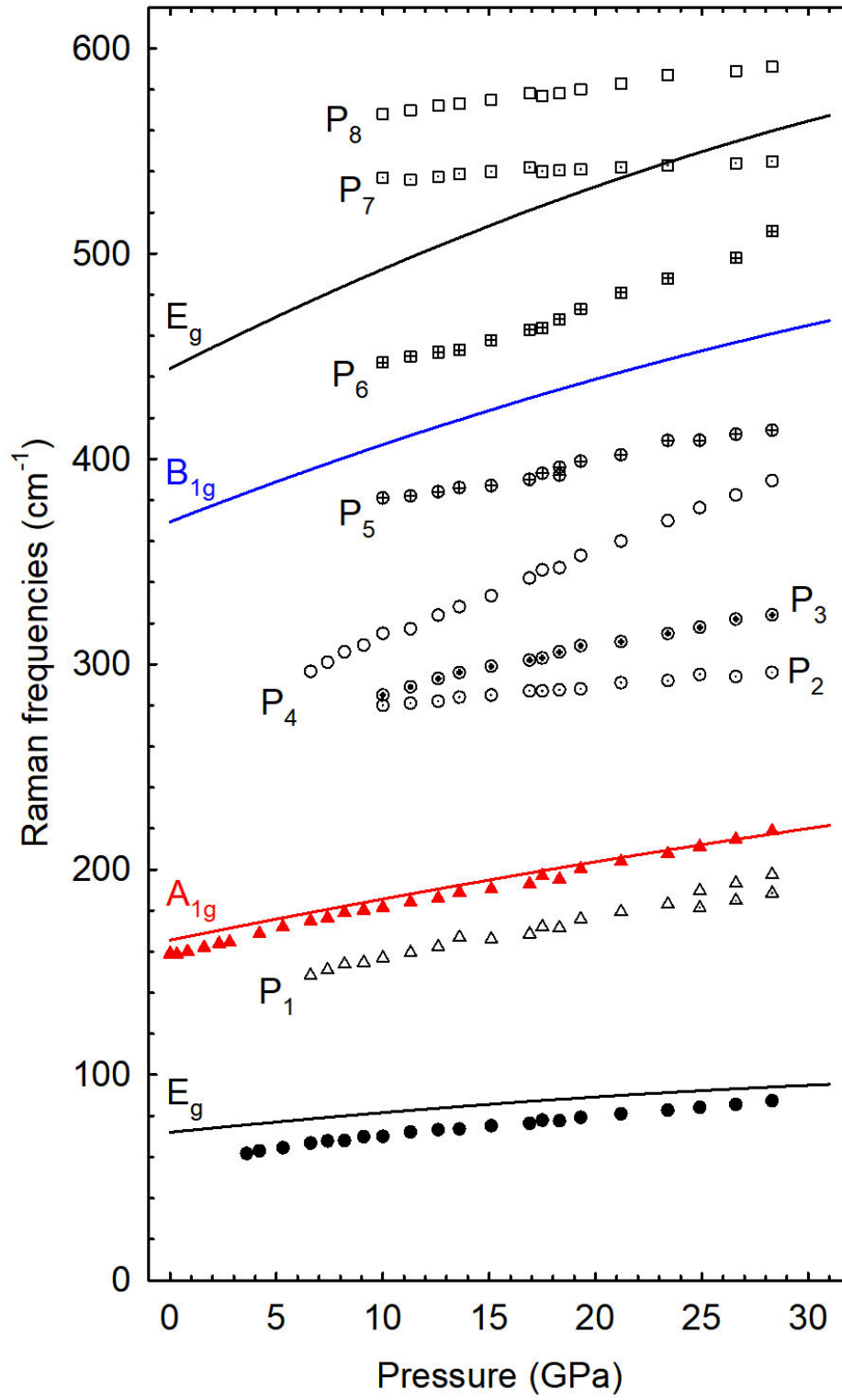
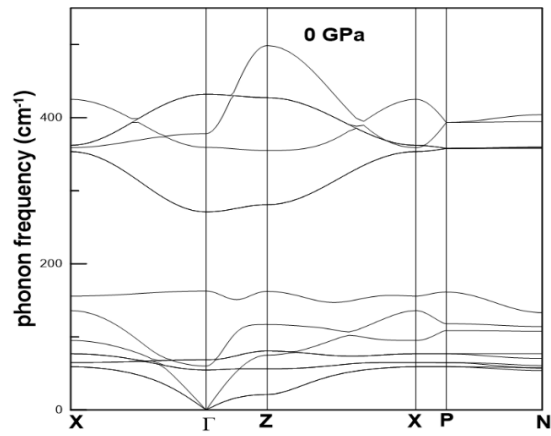
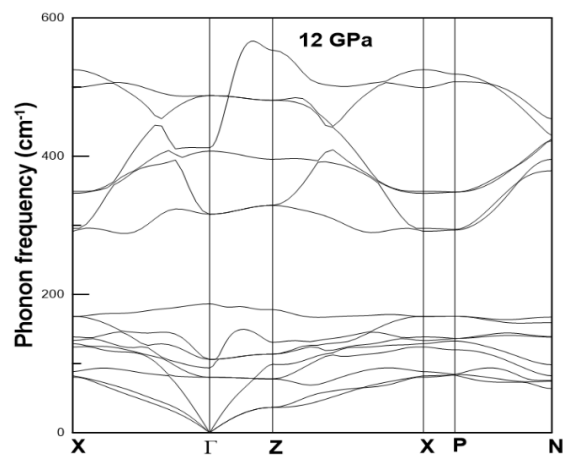


Figure 6

(top)



(center)



(bottom)

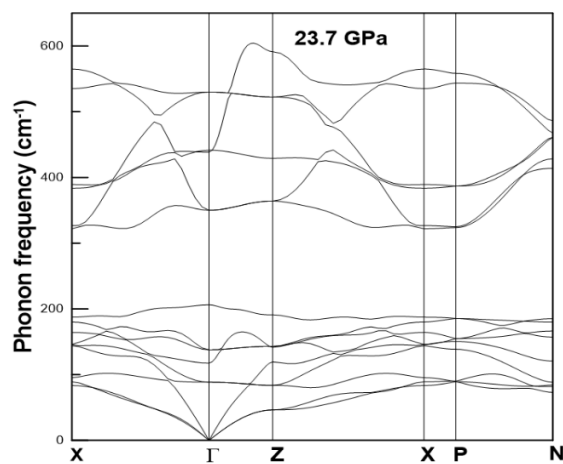


Figure 7

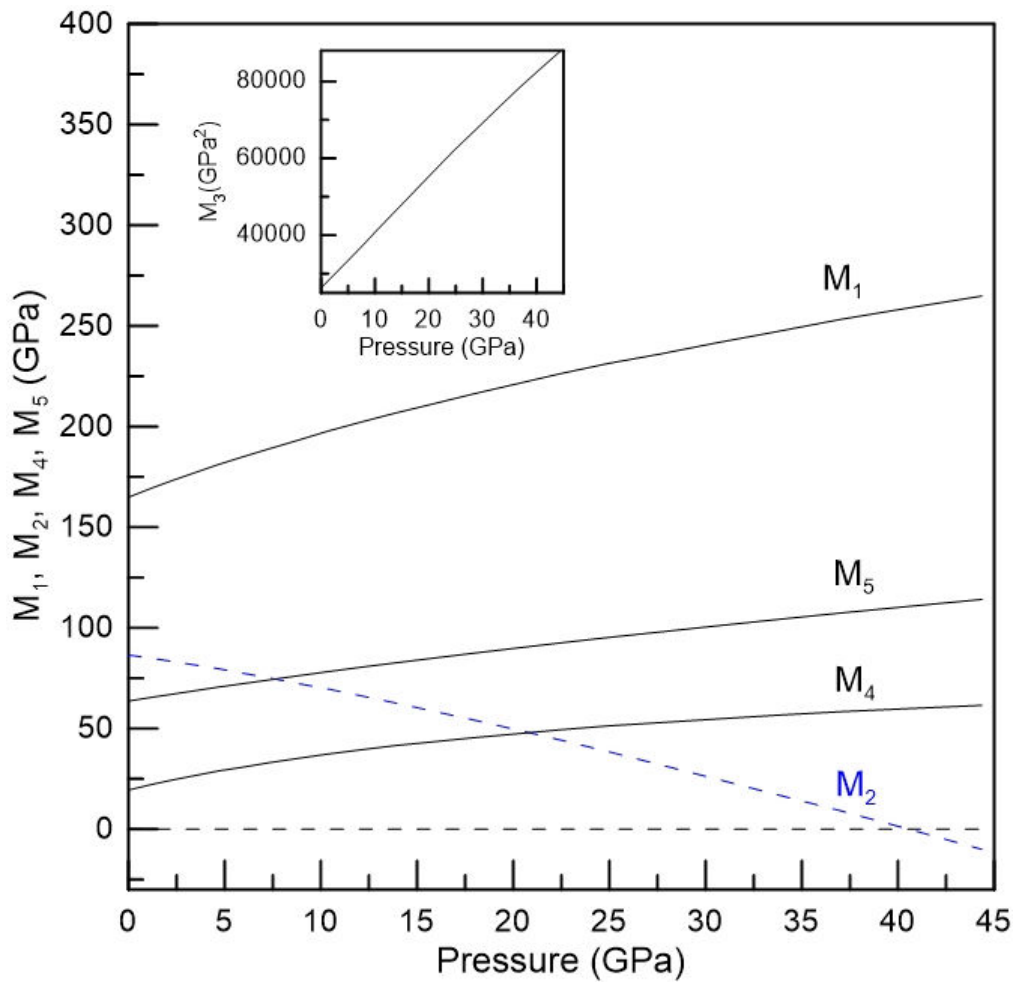


Figure 8

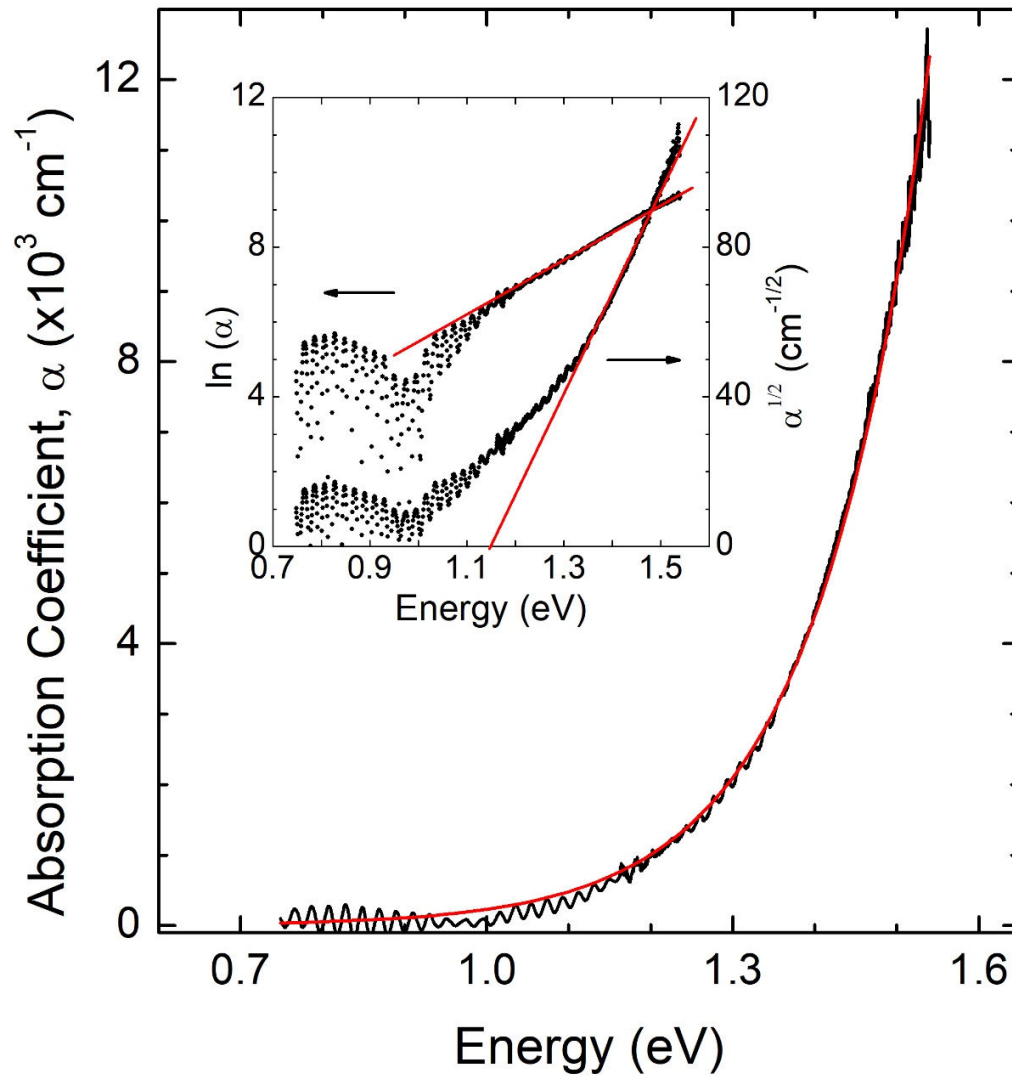
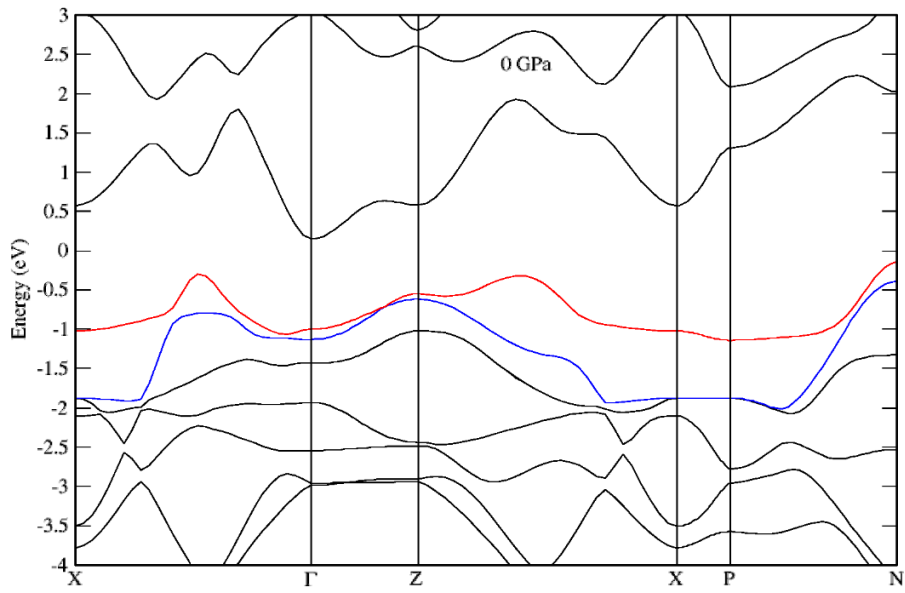


Figure 9

(top)



(bottom)

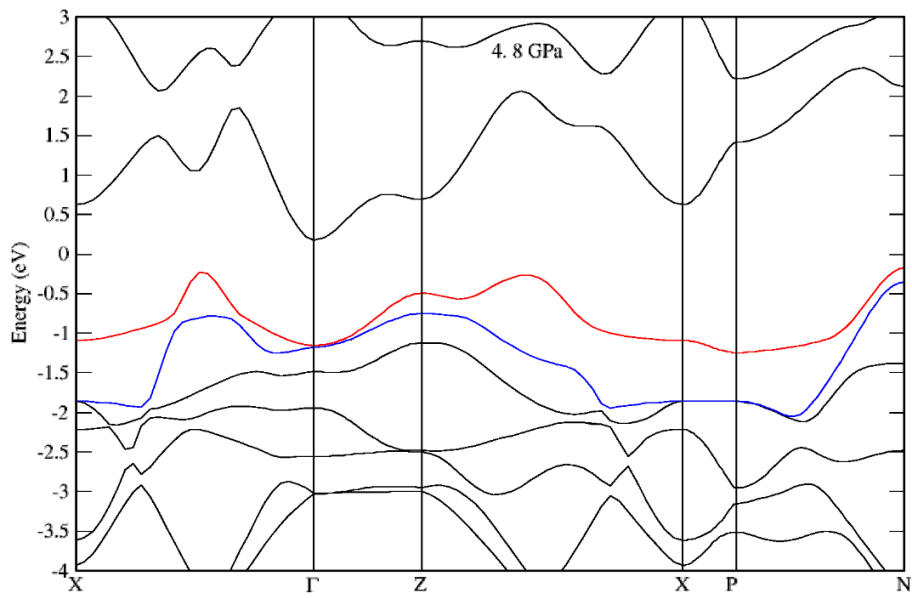


Figure 10

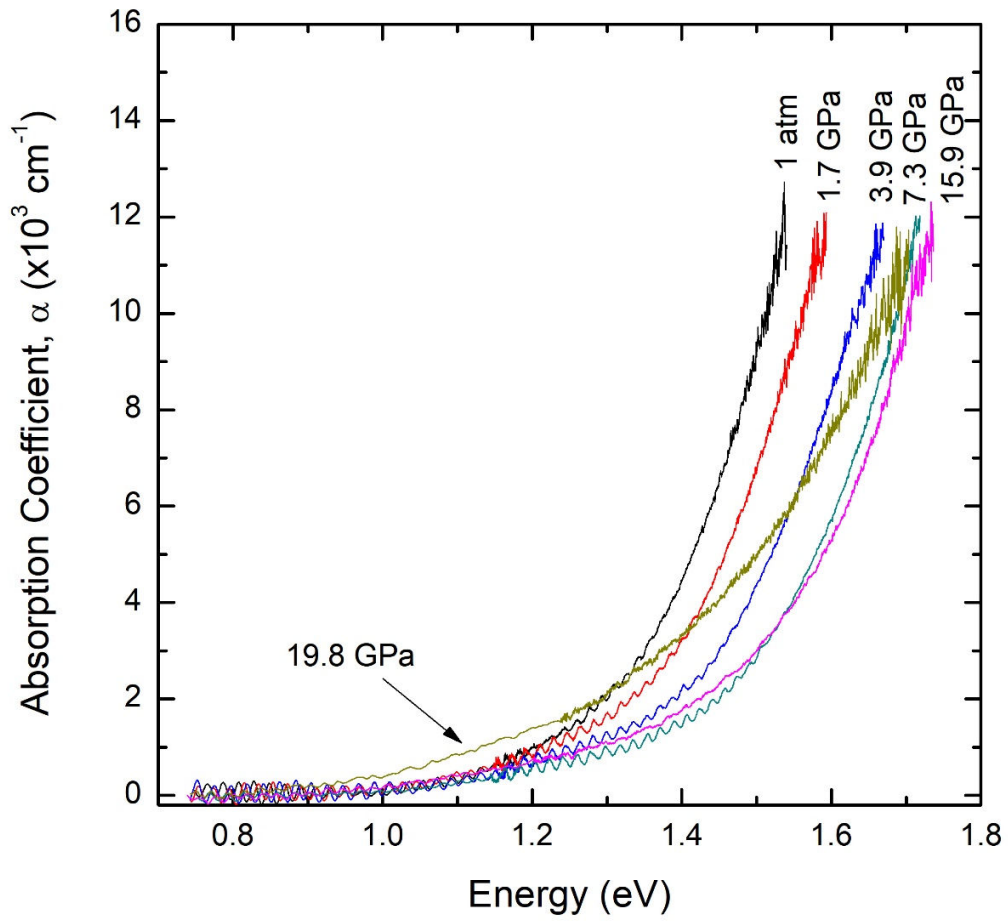


Figure 11

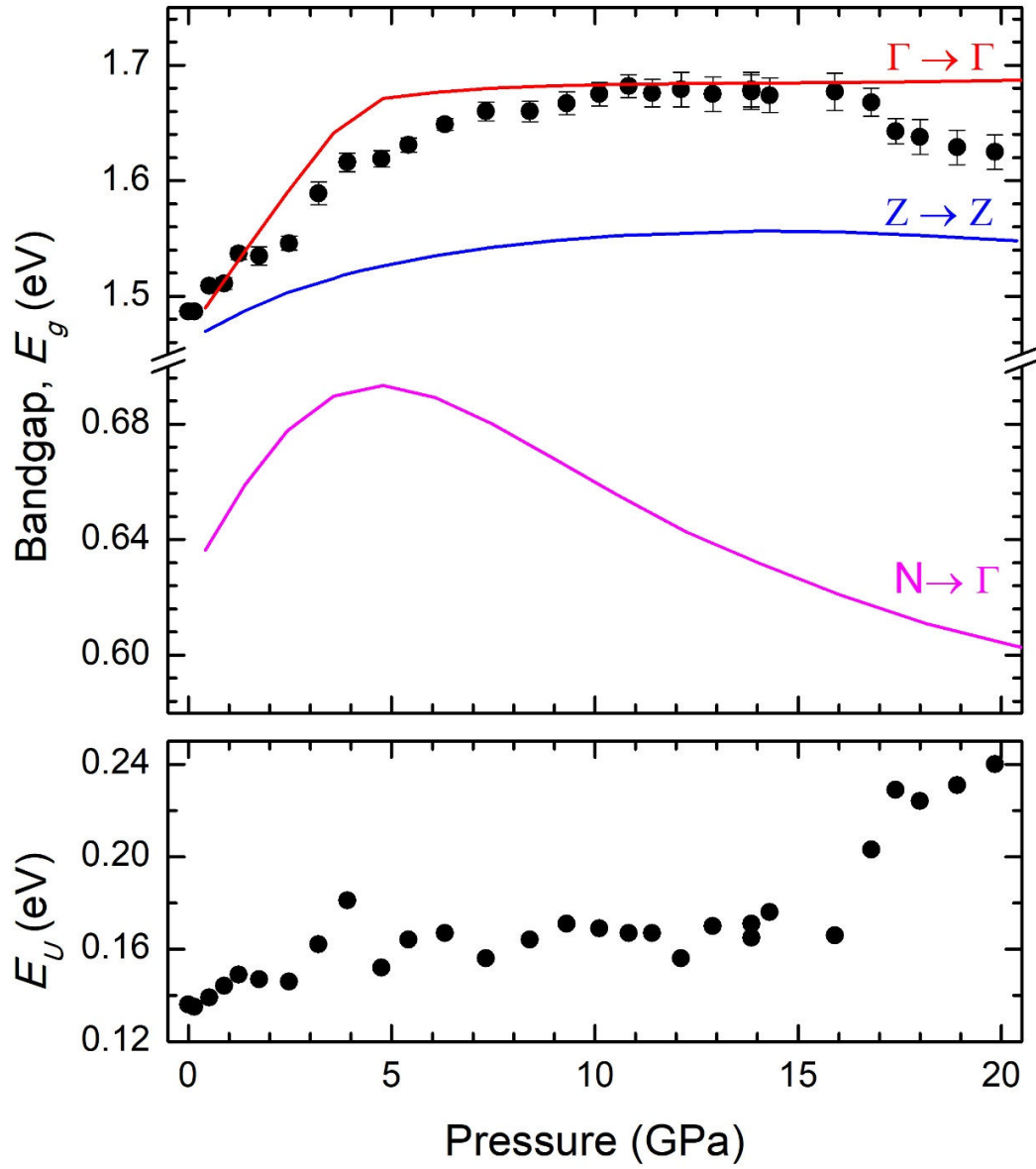


Figure 12 (left)

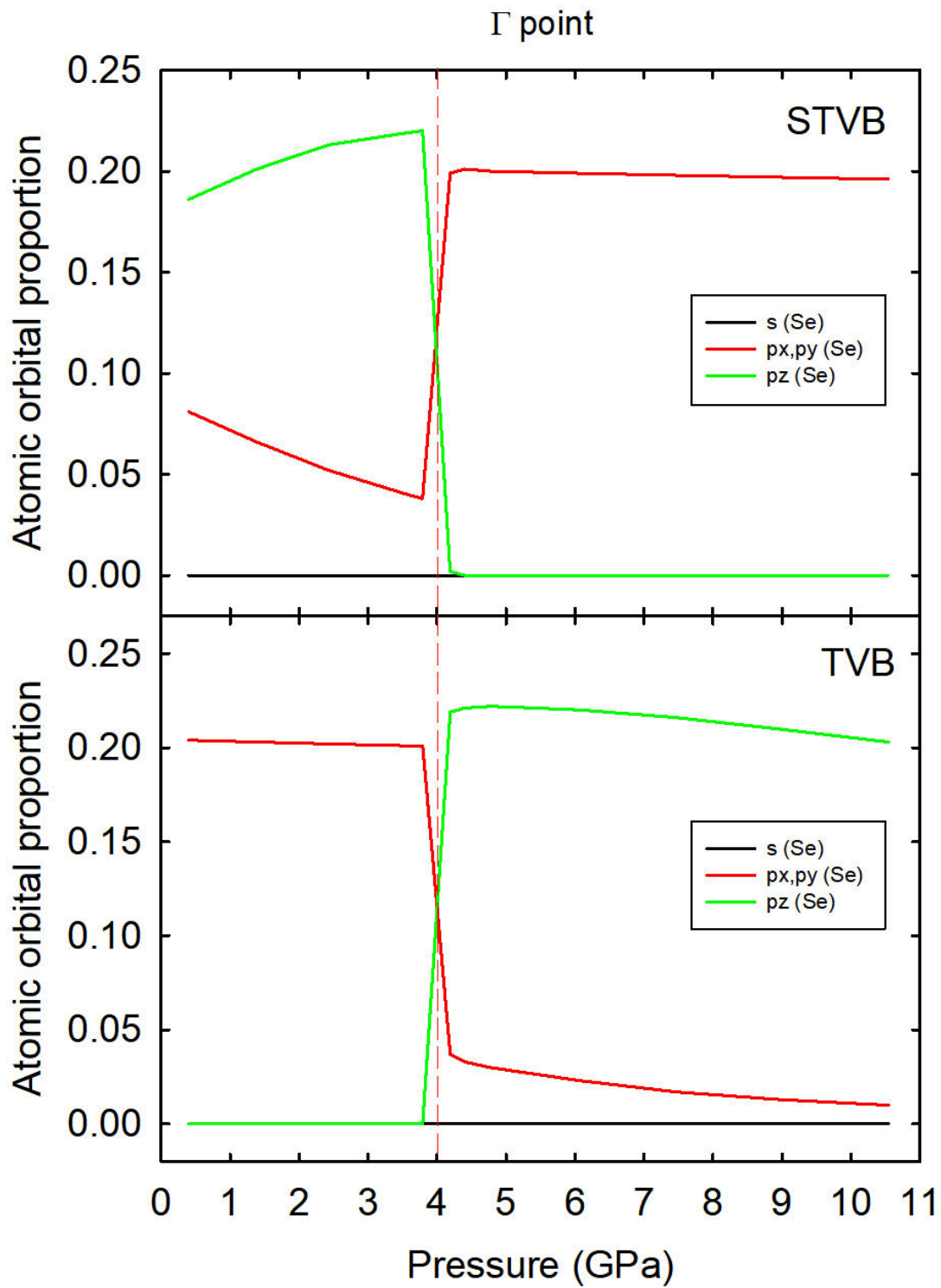
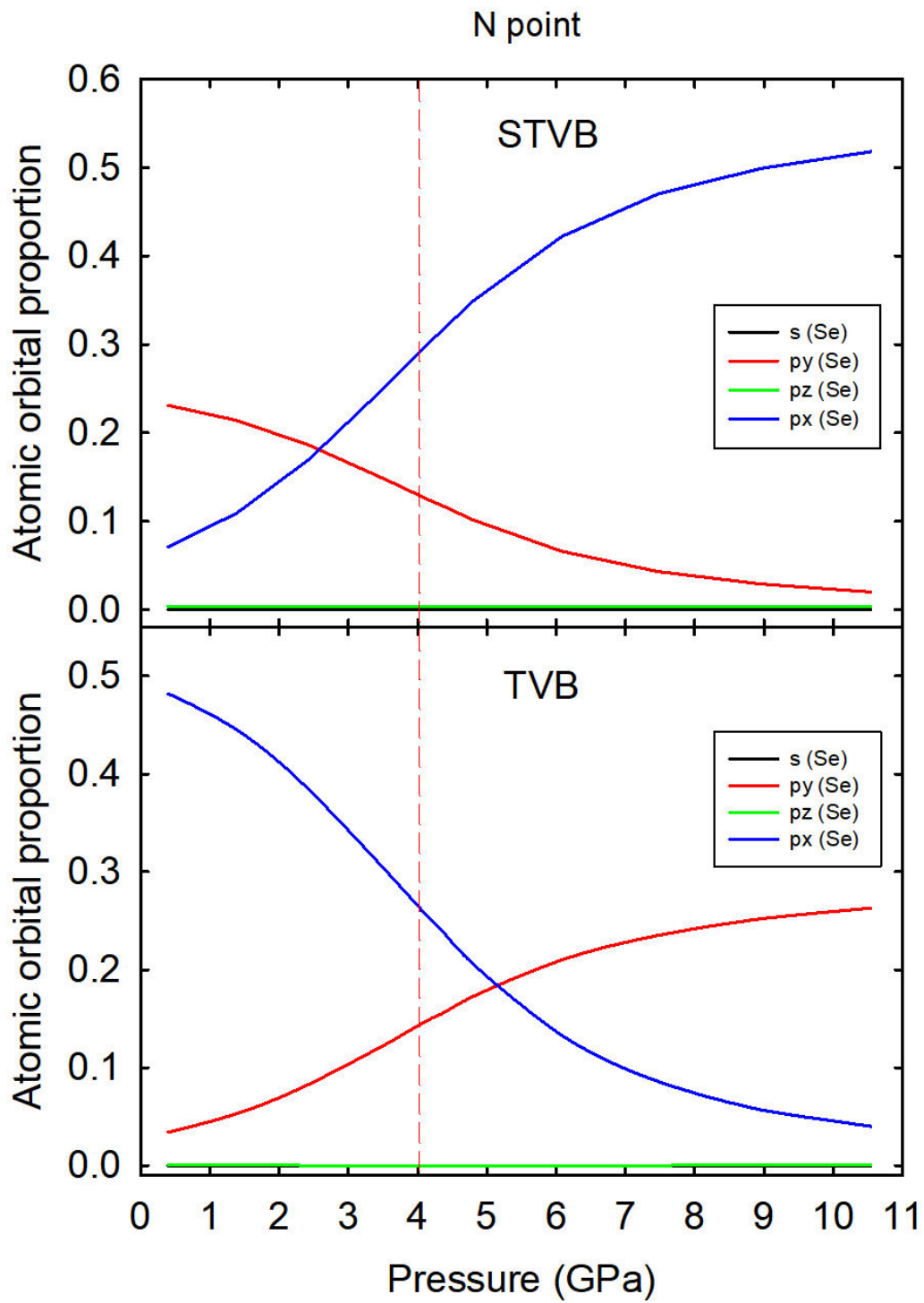
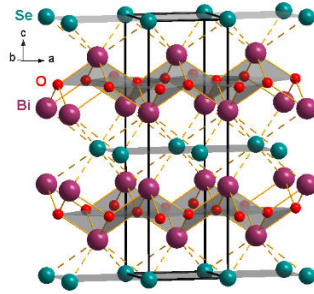


Figure 12(right)



TOC Graphic



Supplementary Material
of
Experimental and Theoretical Study of Bi₂O₂SE Under
Compression

A.L.J. Pereira,^{1,2*} D. Santamaría-Pérez,³ J. Ruiz-Fuertes,^{3,4} F.J. Manjón,^{1*} V.P. Cuenca-Gotor,¹ R. Vilaplana,⁵ O. Gomis,⁵ C. Popescu,⁶ A. Muñoz,⁷ P. Rodríguez-Hernández,⁷ A. Segura,³ L. Gracia,⁸ A. Beltrán,⁹ P. Ruleova,¹⁰ C. Drasar¹⁰ and J. A. Sans¹

¹ *Instituto de Diseño para la Fabricación y Producción Automatizada, MALTA Consolider Team, Universitat Politècnica de València, València, Spain*

² *Grupo de Pesquisa de Materiais Fotonicos e Energia Renovável - MaFER, Universidade Federal da Grande Dourados, Dourados, MS, Brazil*

³ *Departament de Física Aplicada – ICMUV, MALTA Consolider Team, Universitat de València, Burjassot, Spain*

⁴ *DCITIMAC, MALTA Consolider Team, Universidad de Cantabria, Santander, Spain*

⁵ *Centro de Tecnologías Físicas, MALTA Consolider Team, Universitat Politècnica de València, València, Spain*

⁶ *CELLS-ALBA Synchrotron Light Facility, 08290 Cerdanyola, Barcelona, Spain*

⁷ *Departamento de Física, Instituto de Materiales y Nanotecnología, MALTA Consolider Team, Universidad de La Laguna, Tenerife, Spain*

⁸ *Departament de Química Física, MALTA Consolider Team, Universitat de València, Burjassot, Spain*

⁹ *Departament de Química Física i Analítica, MALTA Consolider Team, Universitat Jaume I, Castellón, Spain*

¹⁰ *Faculty of Chemical Technology, University of Pardubice, Pardubice, Czech Republic*

* Corresponding authors, Email: andreperreira@ufgd.edu.br, fjmanjon@fis.upv.es

Structural data of Bi₂O₂Se under pressure

Table S1. Lattice parameters and unit cell volumes of Bi₂O₂Se obtained from synchrotron XRD experiments at different pressures.

P(GPa)	a axis (Å)	c axis (Å)	V (Å ³)
0.49(3)	3.8823(8)	12.184(3)	183.65(9)
0.68(3)	3.8792(7)	12.167(3)	183.10(8)
1.23(3)	3.8718(6)	12.126(2)	181.79(7)
1.47(3)	3.8683(6)	12.106(2)	181.16(7)
1.97(4)	3.8620(5)	12.072(2)	180.05(5)
2.59(3)	3.8543(6)	12.032(3)	178.75(7)
3.00(4)	3.8498(4)	12.004(2)	177.91(4)
3.57(5)	3.8422(6)	11.967(2)	176.66(6)
5.38(6)	3.8231(7)	11.871(3)	173.50(8)
6.01(5)	3.8159(5)	11.832(2)	172.29(7)
6.99(6)	3.8062(5)	11.785(2)	170.73(5)
7.99(7)	3.7982(17)	11.738(6)	169.34(17)
8.5(1)	3.793(2)	11.710(8)	168.5(2)
9.6(2)	3.788(3)	11.675(12)	167.5(3)
11.9(2)	3.7786(18)	11.629(7)	166.03(19)
12.4(2)	3.7754(19)	11.611(8)	165.5(2)
13.2(2)	3.7724(15)	11.591(9)	164.95(19)
14.5(3)	3.770(3)	11.567(12)	164.4(3)
15.2(2)	3.767(3)	11.549(13)	163.9(3)
15.8(3)	3.763(3)	11.526(13)	163.2(3)
16.3(3)	3.761(3)	11.507(13)	162.8(3)
18.2(4)	3.753(4)	11.465(15)	161.4(4)
19.9(4)	3.744(3)	11.422(16)	160.1(4)
21.7(4)	3.735(4)	11.382(19)	158.8(4)

Vibrational modes in Bi₂O₂Se at the Γ point

Bi₂O₂Se crystallizes in the tetragonal body-centered $I4/mmm$ structure and has two formula units in the primitive cell, therefore, it has 10 normal vibrational modes at Γ whose mechanical decomposition is¹:

$$\Gamma = 1 A_{1g}(\text{R}) + 2 A_{2u}(\text{IR}) + 1 B_{1g}(\text{R}) + 2 E_u(\text{IR}) + 2 E_g(\text{R}) + A_{2u} + E_u$$

where A_{1g} , B_{1g} and E_g modes are Raman-active (R) and A_{2u} and E_u are infrared-active (IR). In total, there are four Raman-active modes ($\Gamma_{\text{Raman}} = A_{1g} + B_{1g} + 2E_g$), four infrared-active (IR) modes ($\Gamma_{\text{IR}} = 2A_{2u} + 2E_u$) and two acoustic modes ($\Gamma_{\text{Acoustic}} = A_{2u} + E_u$). It must be mentioned that that E modes are doubly degenerated. The assignment of the vibrational modes to atomic movements can be done thanks to the program J-ICE² that reads OUTCAR files of VASP.

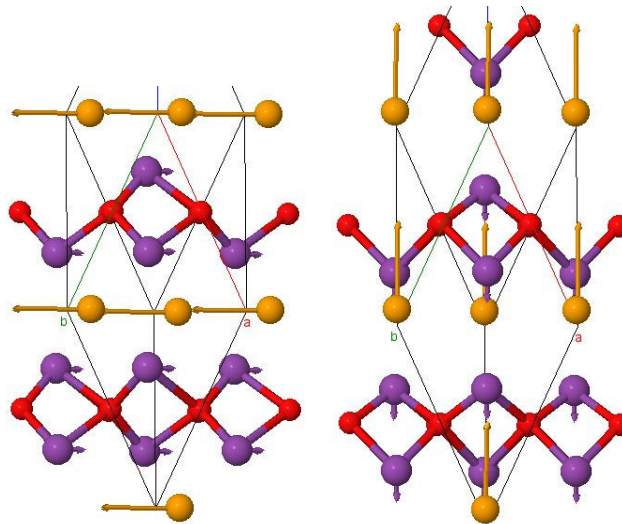


Figure S1. Atomic movements of low-frequency interlayer vibrational modes E_u and A_{2u} .

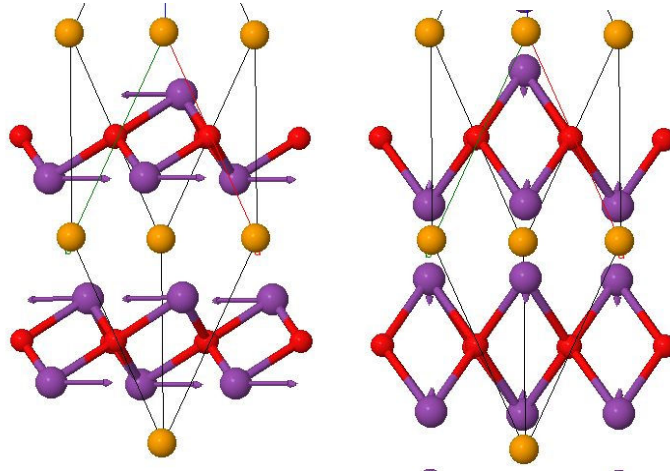


Figure S2. Atomic movements of low-frequency interlayer E_g and A_{1g} vibrational modes.

It is well-known that in layered materials, which usually crystallize either in a hexagonal or tetragonal space group, the lowest-frequency E (doubly degenerated) and A (or B) modes at the Γ point can be classified as interlayer (out-of-phase vibrations of atoms corresponding to adjacent layers) or intralayer (out-of-phase vibrations of atoms inside the layers) modes. Interlayer E and A (or B) modes are usually related to shear or transversal vibrations between adjacent layers along the layer plane (a - b) and to longitudinal vibrations of one layer against the adjacent ones (along the c axis), respectively. Both E and A (or B) interlayer modes come from transversal acoustic (TA) and longitudinal acoustic (LA) modes, respectively, due to the folding of points of the Brillouin zone border into the Γ point due to the decreasing symmetry from cubic to hexagonal or tetragonal. Similarly, E and A (or B) intralayer modes come from transversal optic (TO) and longitudinal optic (LO) modes at Γ and from additional modes due to the folding of the BZ border into the Γ point.

The number of interlayer and intralayer modes in layered materials depends on the complexity of the unit cell. In the simplest case, there should be two interlayer modes and four intralayer modes. In the case of $\text{Bi}_2\text{O}_2\text{Se}$, there are four interlayer modes (E_u , A_{2u} , E_g and A_{1g}) having the lowest frequencies, while the four intralayer modes (E_u , B_g , A_{2u} and E_g) have the highest frequencies. The two modes with lowest frequency, E_u and A_{2u} , are IR-active and correspond to out-of-phase movements of Se and Bi atoms (see **Fig. S1**); i.e. both modes are typical interlayer modes of layered structures. In fact, they correspond to the shear mode between Bi_2O_2 and Se layers in the layer plane and to

the longitudinal vibration of the Bi_2O_2 and Se layers one against the other along the c axis (perpendicular to the layer plane). On the other hand, the low-frequency E_g and A_{1g} modes are Raman-active and correspond to out-of-phase Bi movements in the layer plane and perpendicular to the layer plane, respectively (see **Fig. S2**). These two modes are not so typical of layered materials and come from the fact that there are two Bi_2O_2 layers in the unit cell so that these two modes can be considered as the complementary movements of Bi atoms in the two low-frequency E_u and A_{2u} modes. In these two modes, there is an in-phase movement of Bi atoms in a Bi_2O_2 layer, while in the two low-frequency E_g and A_{1g} modes there is an out-of-phase movement of Bi atoms in the layer. Therefore, the two low-frequency E_u and A_{2u} modes are proper interlayer modes between Bi_2O_2 and Se layers, while the two low-frequency E_g and A_{1g} modes are half interlayer modes between Bi_2O_2 and Se layers and half interlayer modes between the upper and lower halves of each Bi_2O_2 layer.

In layered compounds with typical van der Waals gap between the layers, the low-frequency interlayer shear mode exhibits a much smaller pressure coefficient than other modes, whereas the low-frequency A (or B) mode displays the largest pressure coefficient. For example, the E and A modes with frequencies around 40 (60) cm^{-1} and 116 (133) cm^{-1} in InSe (GaSe) have pressure coefficients of 0.68 (0.85) $\text{cm}^{-1}/\text{GPa}$ and 5.41 (5.78) $\text{cm}^{-1}/\text{GPa}$, respectively^{3,4}. Usually, the small pressure coefficient of the low-frequency E mode in layered materials is ascribed to the weak bending force constant due to weak van der Waals forces between the neighboring layers. On the other hand, the large pressure coefficient of the low-frequency A mode is due to the extraordinary increase of the stretching force constant between neighboring layers due to the strong decrease of the interlayer distance^{3,4}. A similar behavior is found in layered topological insulators Bi_2Se_3 , Bi_2Te_3 and Sb_2Te_3 ⁵⁻⁷. However, a different behavior was recently observed in layered BiTeBr and BiTeI , which also feature a van der Waals gap between the layers⁸. In these semiconductors, the low-frequency $E_1(\text{TO})$ mode has a similar pressure coefficient (4.3 and 3.5 $\text{cm}^{-1}/\text{GPa}$, respectively) than the rest of the optic modes and the low-frequency $A_1(\text{TO})$ mode has not so large pressure coefficient (4.5 and 4.6 $\text{cm}^{-1}/\text{GPa}$, respectively) as expected for a van der Waals compound. This result suggests that interlayer forces in these two compounds are stronger than common van der Waals forces in other layered compounds, likely due to the asymmetry of the layers what causes a strong polarity of bismuth tellurohalides⁹. Moreover, the rather similar pressure

coefficients of these two modes in BiTeBr and BiTeI also suggests that bending and stretching interlayer bonds tend to harden at similar rates with pressure in both compounds; i.e., the anisotropy in the properties along the layers and perpendicular to the layers is not so high as in other layered compounds and tend to disappear at a similar rate with increasing pressure in both compounds.

The case of Bi₂O₂Se is similar to that of BiTeBr and BiTeI because both interlayer E_u and A_{2u} modes show pressure coefficients of 5.5 and 4.1 cm⁻¹/GPa, respectively. **Figure S3** shows the pressure dependence of the theoretical IR-active modes of Bi₂O₂Se. Therefore, the same explanation already given for the interlayer modes in BiTeBr and BiTeI seems to be valid for Bi₂O₂Se; i.e. interlayer bonding forces are of the same order or stronger than in polar van der Waals compounds, like BiTeBr and BiTeI, and clearly much larger than in non-polar van der Waals compounds, like GaSe and InSe. Curiously, the two interlayer E_g and A_{1g} modes in Bi₂O₂Se have pressure coefficients of 1.1 and 2.1 cm⁻¹/GPa. In this case, the shear mode has a small pressure coefficient as in van der Waals compounds, but the longitudinal mode has a very small pressure coefficient as compared to van der Waals compounds. In summary, we can say that both shear interlayer modes (E_u and E_g) and longitudinal interlayer modes (A_{2u} and A_{1g}) have an average pressure coefficient around 3.2 cm⁻¹/GPa in Bi₂O₂Se, thus suggesting that this is a 2D material with bonding interlayer forces between Bi₂O₂ and Se layers considerably stronger than common van der Waals layered compounds.

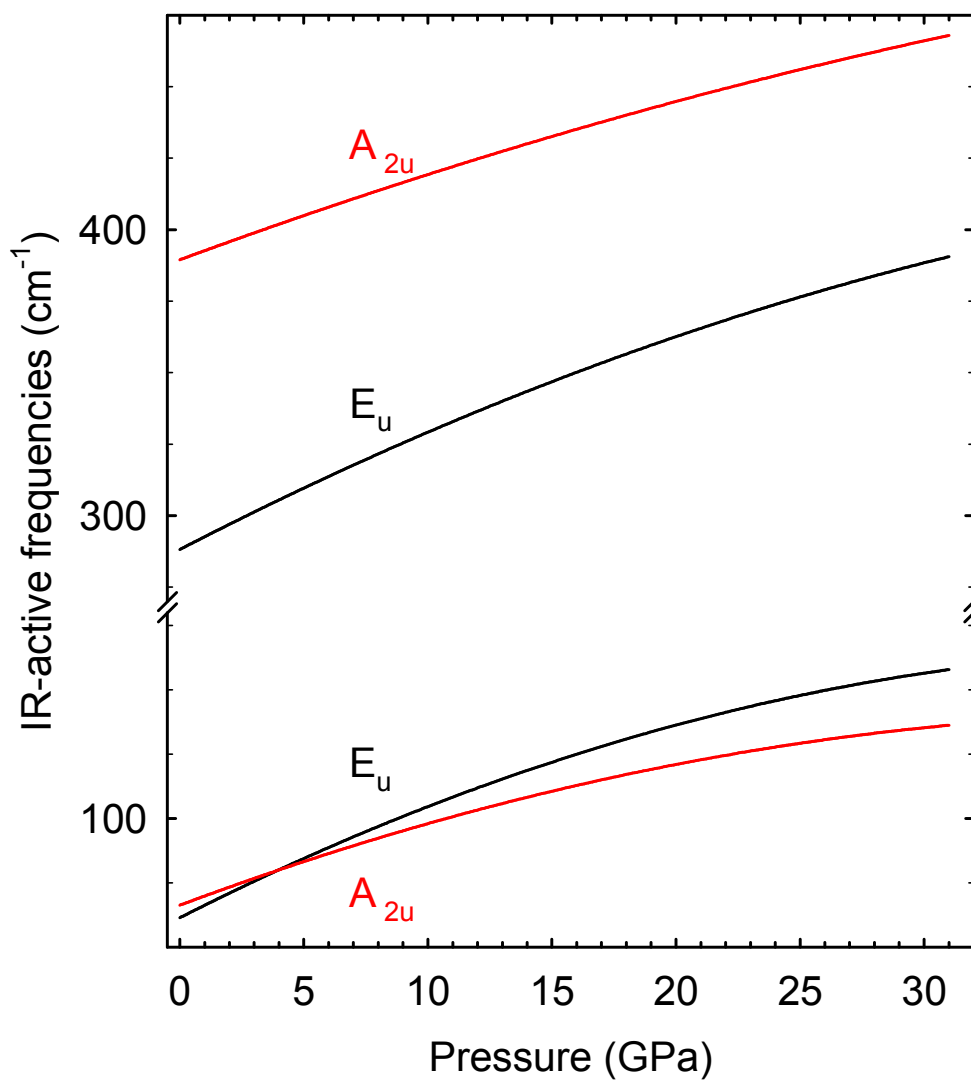


Figure S3. Theoretical pressure dependence of the IR-active modes of Bi₂O₂Se. Different colors represent IR-active modes of different symmetries.

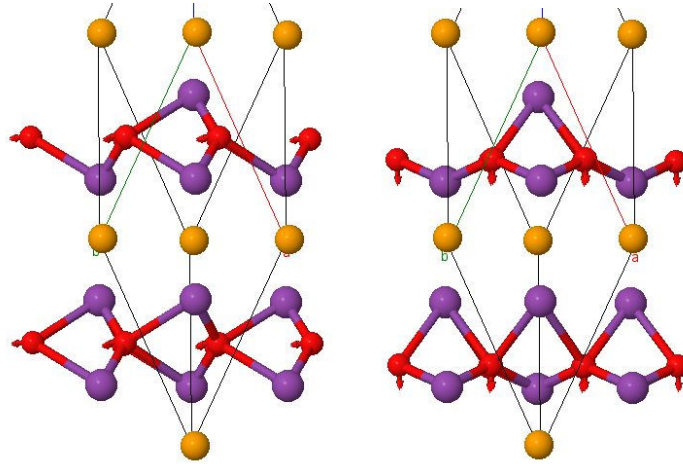


Figure S4. Atomic movements of high-frequency intralayer E_u and A_{2u} vibrational modes.

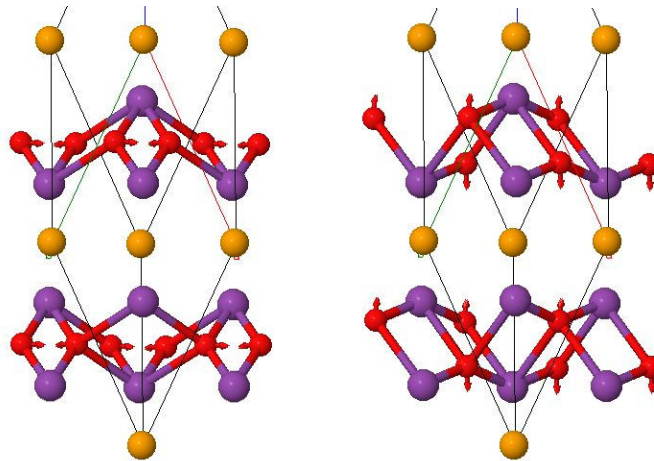


Figure S5. Atomic movements of high-frequency intralayer E_g and B_g vibrational modes.

As regards the high-frequency modes in $\text{Bi}_2\text{O}_2\text{Se}$, they are intralayer modes related to atomic vibrations of O atoms inside the Bi_2O_2 layers. The two high-frequency E_u and A_{2u} modes are IR-active and correspond to in-phase movements of O atoms in the layer plane and perpendicular to the layer plane, respectively (see **Fig. S4**) and E_g and B_g modes are Raman-active and correspond to out-of-phase movements of O atoms inside the Bi_2O_2 layer in the layer plane and perpendicular to the layer plane, respectively (see **Fig. S5**). As regards the pressure coefficients of all these intralayer modes, they are between 3.0 and 5.3 $\text{cm}^{-1}/\text{GPa}$ which are typical of bending and stretching modes of ionic-covalent bonds as the Bi-O bonds in Bi_2O_3 ^{10,11}. In fact, the average pressure coefficient of the transversal and longitudinal modes is 3.7 and 2.9 cm^{-1}

$1/\text{GPa}$, which are values that are in good agreement with the largest value of transversal than longitudinal modes in most ionic-covalent semiconductors¹².

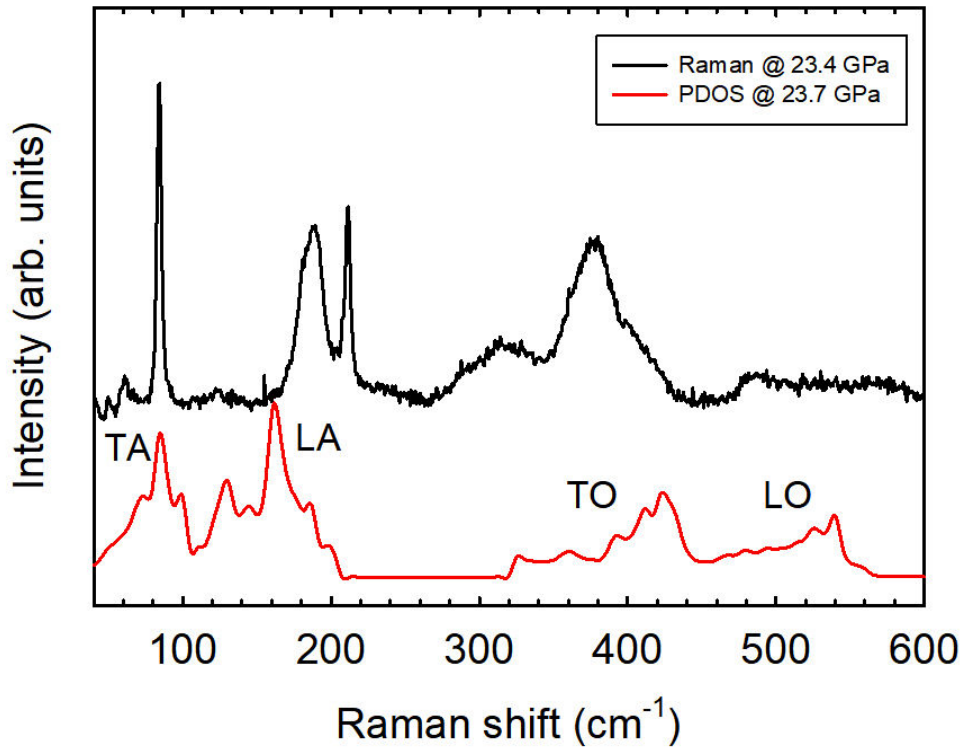


Figure S6. Comparison of the Raman spectrum of $\text{Bi}_2\text{O}_2\text{Se}$ at 23.4 GPa and the theoretical one-phonon density of states at 23.7 GPa.

The RS spectrum of $\text{Bi}_2\text{O}_2\text{Se}$ at 23 GPa shows the two narrow first-order Raman peaks E_g and A_{1g} near 85 and 215 cm^{-1} , respectively. The comparison of RS spectra at 23 GPa with the one-phonon density of states (PDOS) suggests that the other broad bands could originate from one-phonon density of states due to defect assisted Raman scattering. In particular, the broad band at $180\text{-}190 \text{ cm}^{-1}$ could be assigned to the scattering from the top phonon band of the acoustic region (below 210 cm^{-1}) that corresponds to the longitudinal acoustic (LA) region in binary semiconductors. On the other hand, the broad band between 260 and 450 cm^{-1} could be likely assigned to the scattering of the optic transversal (TO) region and other weaker bands at higher frequencies could be likely due to the scattering of the optic longitudinal (LO) region. No clear sign of the PDOS related to the TA region seems to be observed in the RS spectrum.

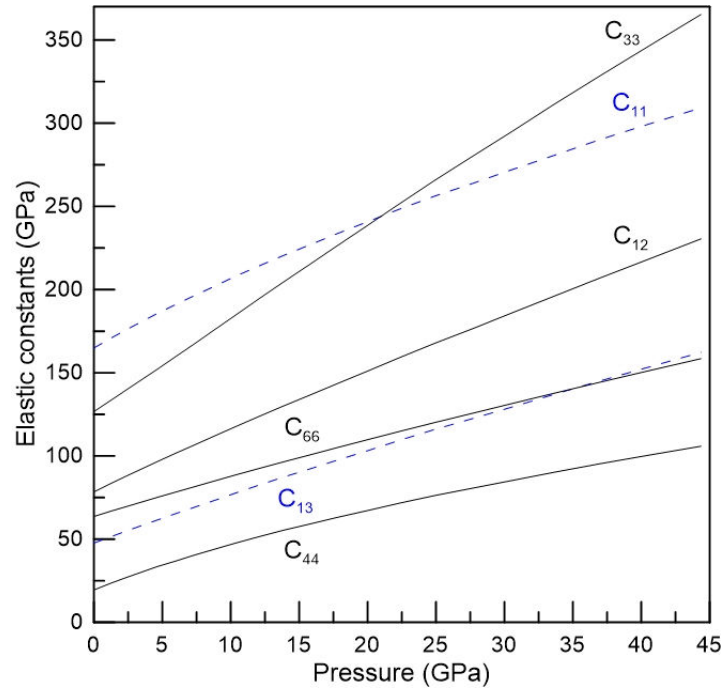


Figure S7. Pressure dependence of theoretical elastic constants, C_{ij} , calculated with VASP in $\text{Bi}_2\text{O}_2\text{Se}$.

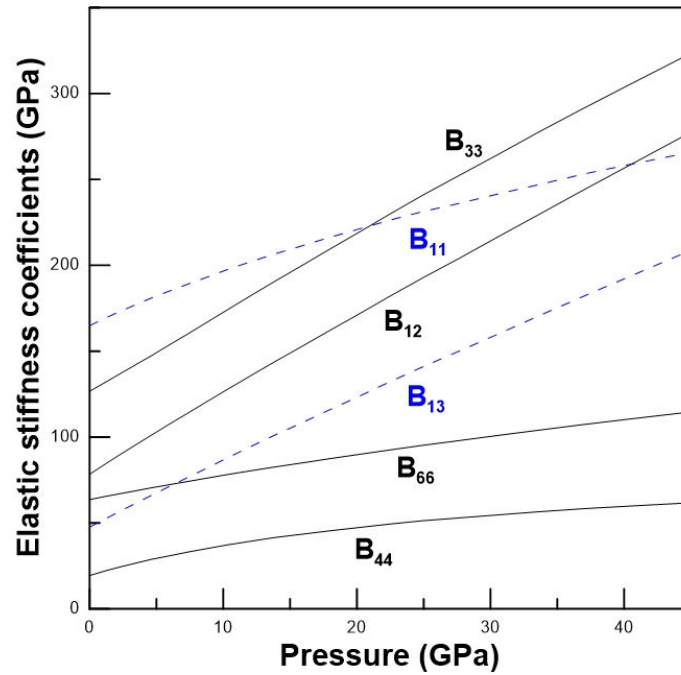


Figure S8. Pressure dependence of theoretical elastic stiffness coefficients, B_{ij} , calculated with VASP in $\text{Bi}_2\text{O}_2\text{Se}$.

The generalized stability criteria for a body-centered tetragonal lattice^{13,14} are given by:

$$M_1 = C_{11} - P > 0$$

$$M_2 = C_{11} - C_{12} - 2P > 0$$

$$M_3 = (C_{33} - P)(C_{11} + C_{12}) - 2(C_{13} + P)^2 > 0$$

$$M_4 = C_{44} - P > 0$$

$$M_5 = C_{66} - P > 0$$

Density of States of Bi₂O₂Se

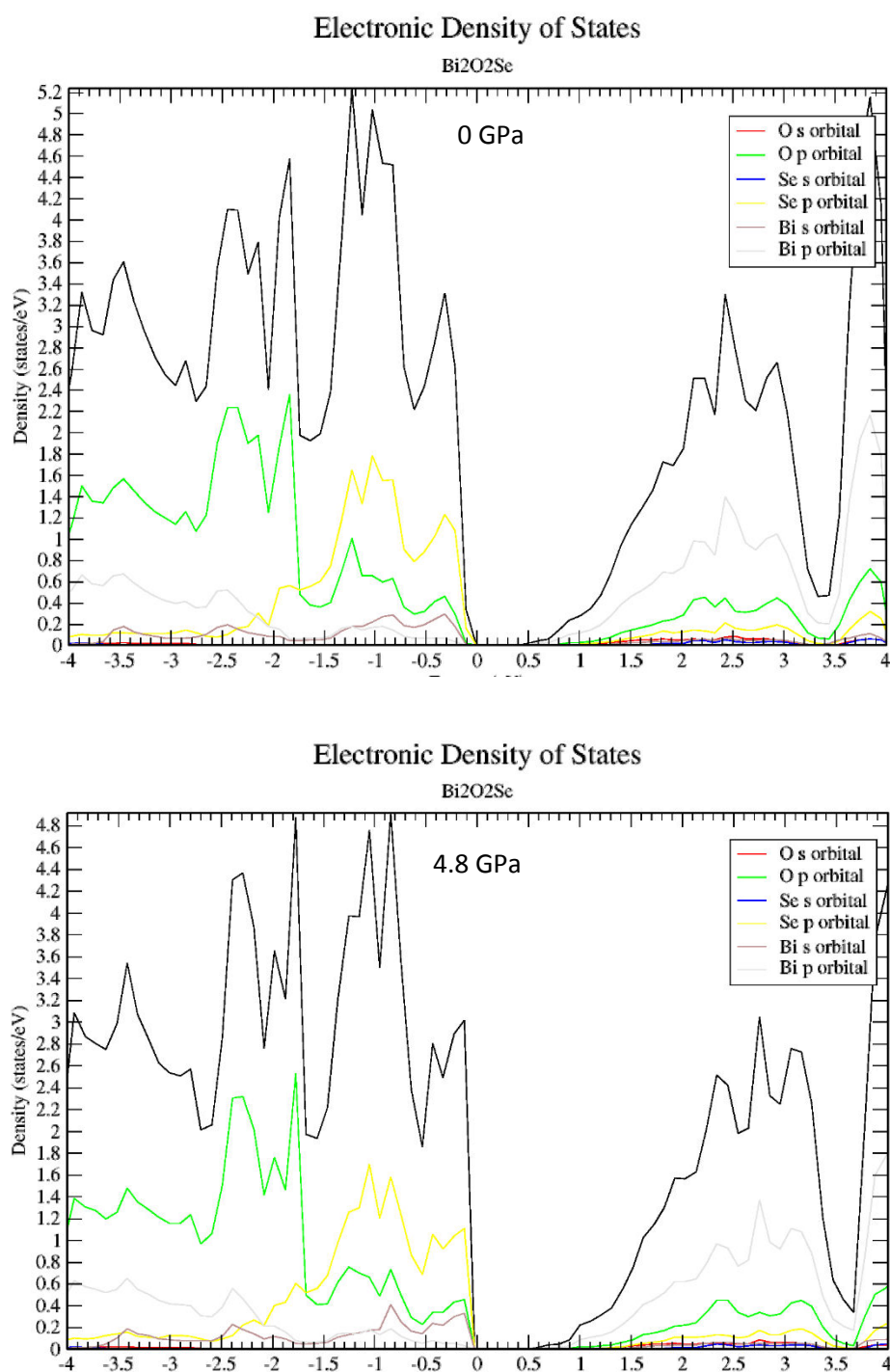


Figure S9. Electronic density of states (DOS) at 0 and 4.8 GPa showing the change of the bandgap with pressure in Bi₂O₂Se.

References

1. Kroumova, E.; Aroyo, M. I.; Perez Mato, J. M.; Kirov, A.; Capillas, C.; Ivantchev, S.; Wondratschek, H. Bilbao Crystallographic Server: Useful Databases and Tools for Phase Transitions Studies. *Phase Trans.* **2003**, *76*, 155-170.
2. Canepa, P.; Hanson, R. M.; Ugliengo, P.; Alfredsson, M. J-ICE: A New Jmol Interface for Handling and Visualizing Crystallographic and Electronic Properties. *J. Appl. Cryst.* **2011**, *44*, 225-229.
3. Ulrich, C.; Mroginski, M. A.; Goñi, A. R.; Cantarero, A.; Schwarz, U.; Muñoz, V.; Syassen, K. Vibrational Properties of InSe under Pressure: Experiment and Theory. *Phys. Stat. Sol. (b)* **1996**, *198*, 121-127.
4. Kulibekov, A. M.; Olijnyk, H. P.; Jephcoat, A. P.; Salaeva, Z. Y.; Onari, S.; Allakverdiev, K. R. Raman Scattering under Pressure and the Phase Transition in ϵ -GaSe. *Phys. Stat. Sol (b)* **2003**, *235*, 517-520.
5. Vilaplana, R.; Gomis, O.; Manjón, F. J.; Segura, A.; Pérez-González, E.; RodríguezHernández, P.; Muñoz, A.; González, J.; Marín-Borrás, V.; Muñoz-Sanjosé, V.; et al. High-Pressure Vibrational and Optical Study of Bi_2Te_3 . *Phys. Rev. B* **2011**, *84*, 104112.
6. Gomis, O.; Vilaplana, R.; Manjón, F. J.; Rodríguez-Hernández, P.; Pérez-González, E.; Muñoz, A.; Kucek, V.; Drasar, C. Lattice Dynamics of Sb_2Te_3 at High Pressures. *Phys. Rev. B* **2011**, *84*, 174305.
7. Vilaplana, R.; Santamaría-Pérez, D.; Gomis, O.; Manjón, F. J.; González, J.; Segura, A.; Muñoz, A.; Rodríguez-Hernández, E.; Pérez-González, E.; Marín-Borrás, V.; et al. Structural and Vibrational Study of Bi_2Se_3 under High Pressure. *Physical Review B* **2011**, *84*, 184110.

8. Sans, J. A.; Manjón, F. J.; Pereira, A. L. J.; Vilaplana, R.; Gomis, O.; Segura, A.; Muñoz, A.; Rodríguez-Hernández, P.; Popescu, C.; Drasar, C.; et al. Structural, Vibrational, and Electrical Study of Compressed BiTeBr. *Phys. Rev. B* **2016**, *93*, 024110.
9. Ma, Y. D.; Dai, Y.; Wei, W.; Li, X. R.; Huang, B. B. Emergence of Electric Polarity in BiTeX (X = Br and I) Monolayers and the Giant Rashba Spin Splitting. *Phys. Chem. Chem. Phys.* **2014**, *16*, 17603-17609.
10. Pereira, A. L. J.; Gomis, O.; Sans, J. A.; Pellicer-Porres, J.; Manjón, F. J.; Beltran, A.; Rodríguez-Hernandez, P.; Muñoz, A. Pressure Effects on the Vibrational Properties of α -Bi₂O₃: An Experimental and Theoretical Study. *J. Phys.: Cond. Mat.* **2014**, *26*, 225401.
11. Pereira, A. L. J.; Sans, J. A.; Vilaplana, R.; Gomis, O.; Manjón, F. J.; Rodríguez-Hernández, P.; Muñoz, A.; Popescu, C.; Beltrán, A. Isostructural Second-Order Phase Transition of β -Bi₂O₃ at High Pressures: An Experimental and Theoretical Study. *J. Phys. Chem. C* **2014**, *118*, 23189-23201.
12. Manjón, F. J.; Syassen, K.; Lauck, R. Effect of Pressure on Phonon Modes in Wurtzite Zinc Oxide. *High Pressure Research* **2002**, *22*, 299-304.
13. Wallace, D. C. Thermoelasticity of Stressed Materials and Comparison of Various Elastic Constants. *Phys. Rev.* **1967**, *162*, 776-789.
14. Grimvall, G.; Magyari-Köpe, B.; Ozolinš, V.; Persson, K. A. Lattice Instabilities in Metallic Elements. *Rev. Mod. Phys.* **2012**, *84*, 945-986.